ADVANCED MATERIALS
www.advmat.de

Controlling Liquid Crystal Orientations for Programmable Anisotropic Transformations in Cellular Microstructures

Shucong Li, Gabriele Librandi, Yuxing Yao, Austin J. Richard, Alyssha Schneider-Yamamura, Joanna Aizenberg, and Katia Bertoldi**

Geometric reconfigurations in cellular structures have recently been exploited to realize adaptive materials with applications in mechanics, optics, and electronics. However, the achievable symmetry breakings and corresponding types of deformation and related functionalities have remained rather limited, mostly due to the fact that the macroscopic geometry of the structures is generally co-aligned with the molecular anisotropy of the constituent material. To address this limitation, cellular microstructures are fabricated out of liquid crystalline elastomers (LCEs) with an arbitrary, user-defined liquid crystal (LC) mesogen orientation encrypted by a weak magnetic field. This platform enables anisotropy to be programmed independently at the molecular and structural levels and the realization of unprecedented director-determined symmetry breakings in cellular materials, which are demonstrated by both finite element analyses and experiments. It is illustrated that the resulting mechanical reconfigurations can be harnessed to program microcellular materials with switchable and direction-dependent frictional properties and further exploit "area-specific" deformation patterns to locally modulate transmitted light and precisely guide object movement. As such, the work provides a clear route to decouple anisotropy at the materials level from the directionality of the macroscopic cellular structure, which may lead to a new generation of smart and adaptive materials and devices.

1. Introduction

Cellular structures comprising networks of plates/struts connected to form arrays of polygons have attracted great attention because of their remarkable geometry-determined functionalities.[1] These include exotic properties such as negative Poisson's ratio,[2] negative swelling,[3] negative refractive indices,[4,5] as well as high strength-to-weight ratio[6–9] and energy absorption.[10] Significant geometric reconfigurations have recently been introduced by making cellular structures out of stimuli-responsive materials.[11–14] Such symmetry breakings hold promise for the design of smart systems with highly tunable symmetry-dependent optical,[15] frictional,[16] wetting,[17] as well as acoustic properties.[18] However, the range of accessible deformations has mostly been limited to simple contraction/extension and/or bending of the constitutive plates and struts. To unlock more complex deformations at the plate level, sophisticated control over the constituent material anisotropy has to be achieved.

Liquid crystalline elastomers (LCEs) are a unique class of soft materials that combine the elasticity of an elastomer with the molecular anisotropy of the liquid crystalline phase (**Figure 1**A). Such intrinsic molecular anisotropy determined by the mesogenic alignment (referred to as mesogenic director, Figure 1A) enables programming of mechanical deformations through a nematic–isotropic (N–I) phase transition[19,20] in response to various environmental stimuli (e.g., heat,[19] light,[21] electric field,[22] and magnetic field[23,24]). To control the mesogenic alignment and therefore the type of achievable mechanical deformation and symmetry breaking, various methods have been proposed. Surface-based alignment, including photoalignment[25,26] and nano-/microgroove-based alignment,[27,28] has allowed complex patterning of directors in space,[25] but it is most effective in 2D thin film systems. As another route, mechanical shearing obtained either via mechanical stretching[29] or 3D/4D printing[30,31] has been used to fabricate LCE structures with more complex geometries; however, these approaches cannot decouple LCE anisotropy from structural architecture, since they limit the achievable mesogenic alignment only to the shearing direction. Finally, it has been shown that 3D LCE microstructures with arbitrary uniaxial mesogenic alignment can be obtained by applying a magnetic field during polymerization.[32,33] This latter capability opens up the possibility to decouple the materials anisotropy at the molecular scale from the orientation of the cellular structure at the architectural scale, and realize mechanical transformations that are rarely achieved in cellular materials.

Here, we demonstrate that a palette of symmetry breakings can be realized in substrate-attached LCE cellular

S. Li, Y. Yao, J. Aizenberg
Department of Chemistry and Chemical Biology
Harvard University
Cambridge, MA 02138, USA
E-mail: jaiz@seas.harvard.edu
G. Librandi, A. J. Richard, A. Schneider-Yamamura, J. Aizenberg, K. Bertoldi
Harvard John A. Paulson School of Engineering and Applied Sciences
Harvard University
Cambridge, MA 02138, USA
E-mail: bertoldi@seas.harvard.edu
The ORCID identification number(s) for the author(s) of this article can be found under https://doi.org/10.1002/adma.202105024.

DOI: 10.1002/adma.202105024

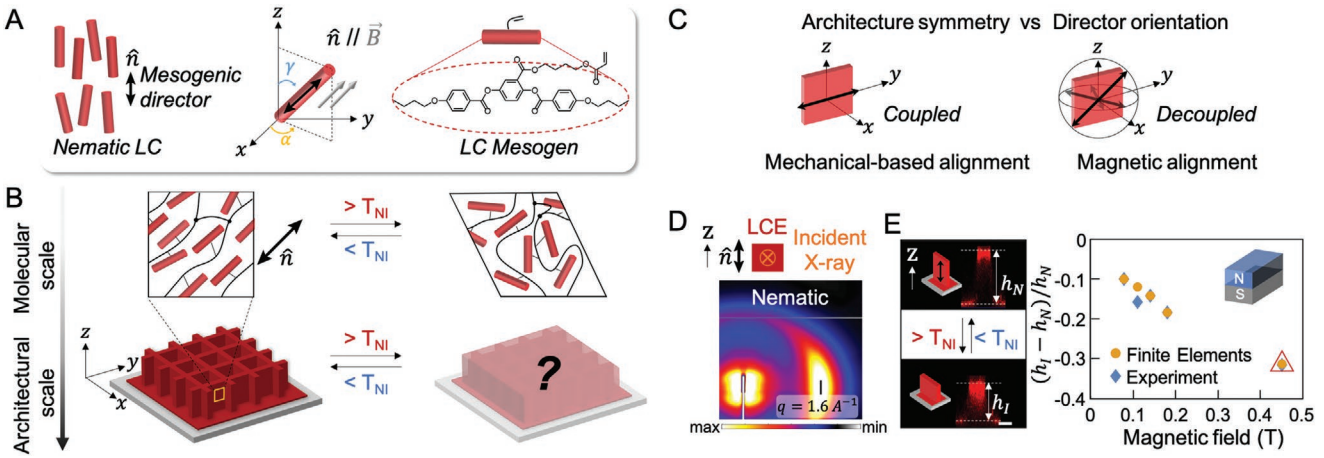

Figure 1. LCE cellular microstructures with decoupled molecular and architectural anisotropy and effect of the magnetic field on the LCE response. A) We use the azimuthal angle α and polar angle γ to denote the mesogenic director of the nematic liquid crystal. Molecular structure of the polymerizable liquid crystalline mesogen is shown on the right. B) The design principle to achieve a palette of symmetry breakings of the LCE cellular structures by independently programming anisotropy at the molecular and architectural scales. C) Mechanical-based alignment (left) does not allow decoupling of LCE anisotropy from structural architecture, as the molecular alignment always follows the stretching direction. By contrast, magnetic alignment (right) permits such decoupling by orienting the object in an arbitrary direction in the magnetic field. D) WAXS patterns of a *z*-aligned LCE block. Note that the incident X-ray is perpendicular to the mesogenic director. E) Left: Fluorescence confocal microscopy images of a *z*-aligned microplate at $T = 25$ °C $< T_{NI}$ (top) and at $T = 135$ °C $> T_{NI}$ (bottom). h_N and h_I denote the height of the plate in the nematic and isotropic phases, respectively. Right: Evolution of the temperature-responsive strain along the molecular director as a function of the strength of the applied magnetic field in LCE fabrication. The diamond and circular markers correspond to experimental data and FE predictions, respectively. The red triangular marker indicates the magnetic field (0.45 T) used in this study for all considered cellular structures.

microstructures by independently programming the anisotropy at the molecular and structural scales (Figure 1B,C). Specifically, we use magnetic field to realize an arbitrary uniaxial mesogenic alignment in the LCE material and study its effect on the deformation modes of microcellular structures with different architectural symmetries. Guided by a systematic understanding of the effect of the magnetic field on the mesogen orientation and the resulting LCE response, as well as Finite Element (FE) simulations, we first consider the vast design space and identify combinations of mesogenic director orientation, lattice symmetry, and lattice connectivity that lead to unexplored pattern transformations, including isotropic/anisotropic buckling, chiral/achiral buckling, tilting, twisting, and shearing. We then demonstrate that such deliberate symmetry breakings can be utilized to program direction-dependent and switchable frictional properties of cellular materials. We further demonstrate the capability to pattern region-specific and gradient director orientations in LCE microcellular surfaces, and exploit the resulting local deformation patterns to realize transmitted light modulation and controlled on-surface object transport. As such, our work provides not only insights in controlling the symmetry breaking in cellular structures, but also a promising platform for the design of the next generation of materials and devices with tunable direction-dependent properties and new functionalities.

2. Results and Discussion

Our LCE microstructures were fabricated out of a monomer mixture consisting of LC mesogens crosslinked with 7.5 wt% of 1,6-hexanediol diacrylate (Figures S1–S3, Supporting Information). We first poured the LC mixture in a negative poly(dimethylsiloxane) (PDMS) mold of the desired microstructure and covered it with a glass substrate (Figures S4 and S5 and Table S1, Supporting Information). We then heated the LC mixture up to $T = 90$ °C to reach its isotropic phase (Figure S3, Supporting Information). Next, we take advantage of the anisotropic magnetic susceptibility of LC monomers of the mixture[34] and use an external magnetic field to align the nematic directors. Specifically, guided by numerical simulations, we positioned the mold in the desired orientation within the magnetic field generated by commercially available magnets to realize an arbitrary, user-defined mesogenic alignment within the cellular microstructures. We then cooled down the unpolymerized mixture with aligned mesogens to its nematic phase (at $T = 60$ °C) and subjected it to UV-polymerization under a nitrogen atmosphere for 30 min.[33] Finally, we cooled down the sample to room temperature, and carefully peeled off the PDMS mold to release the surface-attached LCE microstructure (see Section S1.3.1, Supporting Information for additional details).

To quantify the resulting alignment of mesogens within the cellular structure, we conducted wide-angle X-ray scattering (WAXS) experiments (Figure 1D; Section S1.3.3, Supporting Information). We find that at $T = 60$ °C the scattering from LCE block exhibits a direction-dependent intensity profile with a distinct peak along the equatorial direction at $q = 1.6$ A^{-1}, which corresponds to the distance between neighboring mesogens.[29] Based on these WAXS results, we can estimate the scalar order parameter in the nematic phase to be ≈0.21 (details in Section S1.3.3 and Figure S6, Supporting Information).[35] Hence, using this strategy we can encrypt a user-defined mesogenic alignment to LCE structures with heights up to 1 mm, a size

range that represents a challenge for surface-based alignment methods, which often align micrometer-thick thin films.[25–28]

While the mesogenic alignment is permanently encoded into LCE after polymerization process, the material undergoes nematic–isotropic transition when heated above its N–I phase transition temperature, T_{NI} = 125 °C (Figure S3B, Supporting Information), leading to a reversible, temperature-responsive mechanical actuation (note that the glass transition temperature for our LCEs is T_g = 48 °C, Figure S3B, Supporting Information). As shown in Figure 1E, a surface-attached LCE microplate with size 250 × 50 × 200 µm (length × width × height) synthesized in a low-intensity magnetic field (0.45 T) aligned along its height shortens by $\varepsilon_z = (h_I - h_N)/h_N = -0.32$ (h_N and h_I denoting its height in the nematic and isotropic phases, respectively) upon N–I phase transition, regardless of the temperature ramping rate (see Figure S7, Supporting Information). Importantly, the extent of such deformation can be controlled by varying the intensity of the magnetic field applied during the polymerization process. In particular, we find that ε_z monotonically increases with the intensity of the magnetic field as a stronger magnetic field applied to the unpolymerized mixture leads to a higher scalar order parameter, see Figure 1E and Figure S8, Supporting Information.

While previous studies have investigated the deformation of either cellular structures with the nematic director aligned along the plates[31] or simple shapes with an arbitrary nematic director,[33,36] the interplay between LCE molecular anisotropy and the constraints introduced by the interconnectivity typical of cellular structures can largely expand the range of achievable deformations. To first explore how LCE molecular anisotropy can affect the deformation and symmetry breaking of surface-attached cellular structures, we conducted finite element (FE) simulations using the commercial package ABAQUS 2018/Standard. In all our numerical analyses, we discretized the models with 8-node linear brick solid elements (Figure S9, Supporting Information), and captured the response of LCEs using the strain energy density[37]

$$W = \frac{1}{2}\left[\frac{E}{(1+\nu)(1-2\nu)}\delta_{ij}\delta_{kl} + \frac{E}{1+2\nu}\left(\delta_{ik}\delta_{jl} + \delta_{il}\delta_{jk}\right)\right]\varepsilon_{ij}\varepsilon_{kl} - \frac{\beta}{2}\left(S^t - S^0\right)\left(3n_i n_j - \delta_{ij}\right)\varepsilon_{ij} \quad (1)$$

where ε_{ij} is the Lagrange strain tensor, δ_{ij} is the Kronecker delta and E = 0.4 MPa and ν = 0.49 are the Young's modulus and Poisson's ratio of the LCE, respectively.[38] Further, n_i is the i-th nematic director component, S^0 = 0.21 denotes the initial nematic scalar order parameter and St represents the instantaneous nematic scalar order parameter. Finally, β is a parameter defining the degree of coupling between the elastic strain energy and the potential energy introduced by the nematic order, which we set equal to 0.041 MPa as this value enables us to capture the experimental results reported in Figure 1E. In all our simulations, we assumed perfect bonding between the LCE cellular structures and the substrate and monotonically decreased St from S^0 to 0 to simulate the mechanical deformations arising from the loss of mesogen alignment occurring upon nematic–isotropic phase transition (see Supporting Information Section S2 for details).

To begin with, we focused on a surface-attached square lattice with *P*4*mm* symmetry (**Figure 2**A and Figure S10, Supporting Information).[39] We chose plates with l/h = 0.6 and h/t = 6.67, where l, h, and t denote the length, height and thickness of the plates, respectively, and used FE simulations to systematically explore how molecular anisotropy (i.e., the mesogenic director described by the azimuthal angle α and polar angle γ—Figure 1A) affects their meso-scale deformations. We find that four distinct, elementary deformation modes of cellular microstrucutres emerge when the nematic–isotropic phase transition of the LCE happens (Figure 2B–E). First, when the mesogenic director is along the C_4 rotational axis (i.e., α = 0° and γ = 0°), all plates in the isolated state expand in the x–y plane and shrink along the z axis (Figure 2B-top). While this plate deformation in an isolated square cell leads to a global expansion in the x–y plane (see Figure S11, Supporting Information), it is prevented by the neighbors in the interconnected square lattice. As such, each plate buckles into a half sinusoidal wave and leads to the formation of a wavy pattern with *P*4*gm* symmetry (Figure 2B-center), similar to that previously observed for swollen square lattices made of isotropic materials.[13] Second, when the mesogenic director is in the σ_{v1} mirror plane but tilted 45° away from C_4 axis (i.e., α = 0° and γ = 45°), both the horizontal and vertical plates undergo shearing in the same x–z plane (Figure 2C-top)—a deformation mode that is rarely encountered in microplates and stems from the molecular anisotropy of the constituent LCEs. Since the shearing direction and extent of each plate are compatible with that of the neighbors, similarly to the case of an isolated square cell (see Figure S11, Supporting Information), a rarely encountered global shearing of the interconnected lattice with a symmetry reduction to *Pm* is observed (i.e., only the mirror planes σ_{v1} and σ'_{v1} are preserved from the initial lattice—Figure 2C-center and Figure S11, Supporting Information). Third, when the nematic director is orthogonal to C_4 axis and in the σ_{v1} mirror plane (i.e., α = 0° and γ = 90°) the horizontal plates shrink along the x-axis while the vertical ones expand along the y-axis (Figure 2D-top), so that an isolated square cell transforms into a rectangular one (Figure S11, Supporting Information). However, as observed for α = 0° and γ = 0°, for the cellular structure the expansion of the vertical elements also results in buckling. Differently, the shrinkage of the horizontal plates is prevented by the neighboring elements and results in a tensile state of stress. This behavior leads to an anisotropic buckling pattern with *Pm* symmetry (Figure 2D-center). Fourth, when the mesogenic director is in the σ_{d1} mirror plane and orthogonal to C_4 axis (i.e., α = 45° and γ = 90°), all plates twist (Figure 2E-top and Figure S11, Supporting Information), resulting in a diamond-like pattern with *C*2*mm* point group (Figure 2E-center). Finally, we want to emphasize the deformation shown in Figure 2B–E present four elementary modes, but many more symmetry breaking patterns can be achieved by systematically varying the mesogenic director's orientation (arbitrary angles α and γ) in 3D (Figure S10, Supporting Information). These additional actuation behaviors can be expressed as a combination of the four elementary deformation modes reported in Figure 2. For example, if the nematic director lies in the σ_{v1} mirror plane and is tilted by 22.5° away from C_4 axis (i.e., α = 0° and γ = 22.5°) a buckling instability mixed with a shearing deformation is expected to

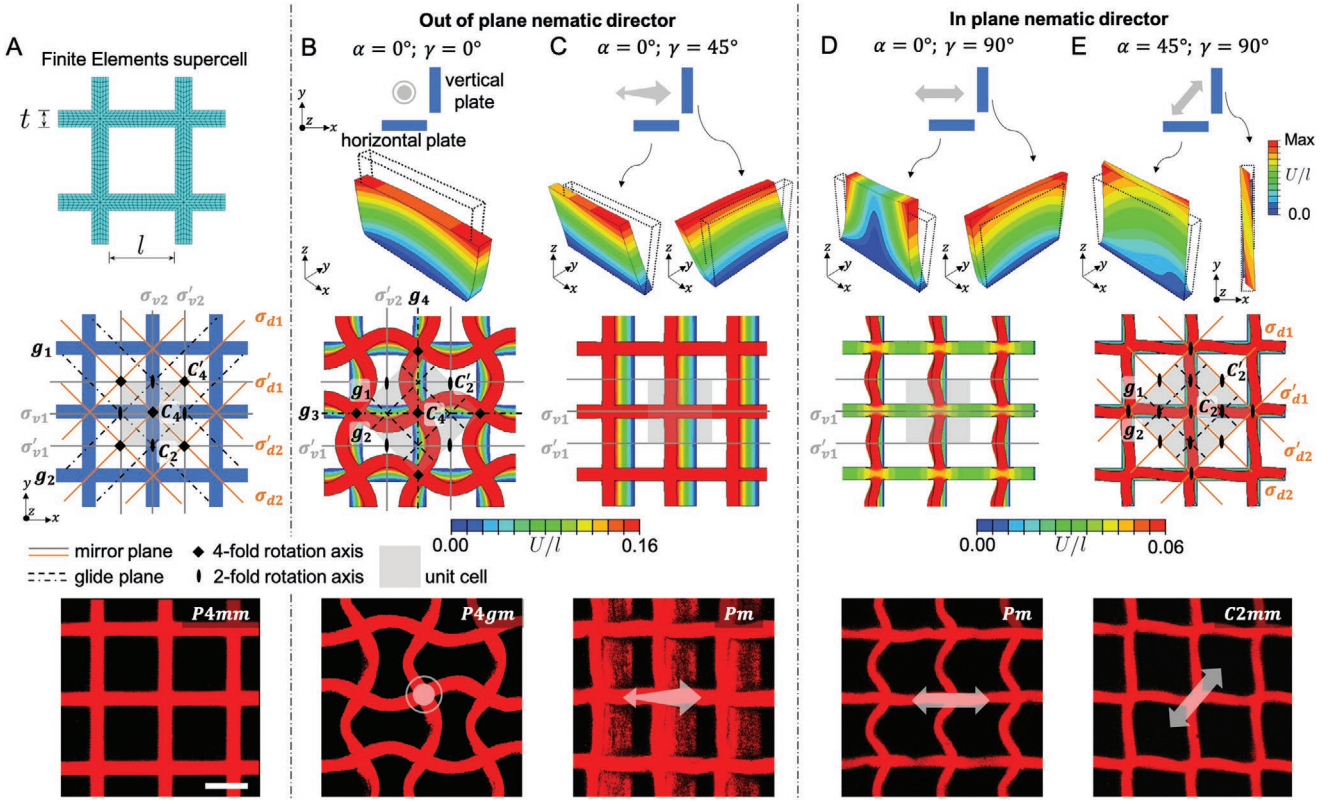

Figure 2. Symmetry breakings for a surface-attached LCE square microlattice. A) Top: FE supercell for deformation calculation. Center: lattice with $l/h = 0.6$ and $h/t = 6.67$ below T_{NI} with symmetric elements marked. Bottom: an experimental confocal microscopy image of undeformed LCE square microlattice. B–E) Deformed lattice above T_{NI} for the case of mesogenic alignment defined by: B) $\alpha = 0°$, $\gamma = 0°$; C) $\alpha = 0°$, $\gamma = 45°$; D) $\alpha = 0°$, $\gamma = 90°$; E) $\alpha = 45°$, $\gamma = 90°$. Top: FE results for isolated LCE microplates above T_{NI}. Center: FE results for an infinitely large square lattice upon N–I phase transition. Bottom: fluorescence confocal microscopy images showing the deformations of the microstructures at $T = 135$ °C $> T_{NI}$. For the FE results, we also show the normalized magnitude of the displacement field in the isotropic phase (displacement U divided by original lattice length l) in different colors. Double-headed gray arrows in the top and bottom row illustrate the projection of the 3D mesogenic director in the xy-plane. Note, the red color of the experimental results comes from the Rhodamine dye on LCE samples and does not reflect the deformation extent as shown in the FE analysis. Scale bar: 50 µm.

occur, whereas for $\alpha = 22.5°$ and $\gamma = 90°$ the lattice will anisotropically twist upon the N–I phase transition (Figure S10, Supporting Information).

To validate the numerical results, we fabricated a square lattice identical to that investigated in Figure 2 with $l = 60$ µm, $t = 15$ µm, and $h = 100$ µm with the method described above (see Section S1.3, Supporting Information for details). Remarkably, for all considered mesogenic directors the samples deformed as predicted by the FE simulations (Figure 2—bottom; Figure S12, Movie S1, and Movie S2, Supporting Information), confirming that the molecular anisotropy encrypted in the LCE relative to the orientation of the structure at the architectural scale can be exploited to program a wide range of deformations and symmetry breaking in microcellular structures. However, while in the FE analysis we apply an infinitesimal perturbation to guide the formation of a single buckling phase, in our experiments multiple (right- and left-handed) buckling phases emerge triggered by several nucleation events (Figure S13, Supporting Information). Finally, we note the bonding between the LCE cellular structures and the substrate significantly affects their deformation behavior, as in the presence of low interfacial adhesion no buckling is observed (Figure S14, Supporting Information).

We next use FE simulations to investigate the response of architectures with different symmetries. Focusing on a *P6mm* triangular lattice structure with $l/h = 1.9$ and $h/t = 4.27$, we find that, when the nematic director is aligned along the z-axis (i.e., $\alpha = 0°$ and $\gamma = 0°$), each plate buckles into a full sinusoidal wave (**Figure** 3A and Movie S2, Supporting Information), resulting in the formation of a chiral pattern.[13] Interestingly, when the nematic director is oriented along the x-axis (i.e., $\alpha = 0°$ and $\gamma = 90°$), the two oblique edges of each triangle twist by the same amount but in the opposite directions, while the horizontal one does not deform significantly, remaining in a tensile state of stress. The latter deformations lead to an achiral hourglass-like pattern not observed in previously reported cellular structures, with a mirror plane σ_v cutting through the nodes (Figure 3B and Movie S2, Supporting Information). Note that in this pattern the angles between neighboring plates at the joints are not preserved, an unusual feature which stems from the molecular anisotropy. Further, more unusual symmetry breakings can be achieved by combining this symmetric twisting with other elementary deformations through the control of the director orientation in the LCE material (Figure S15, Supporting Information).

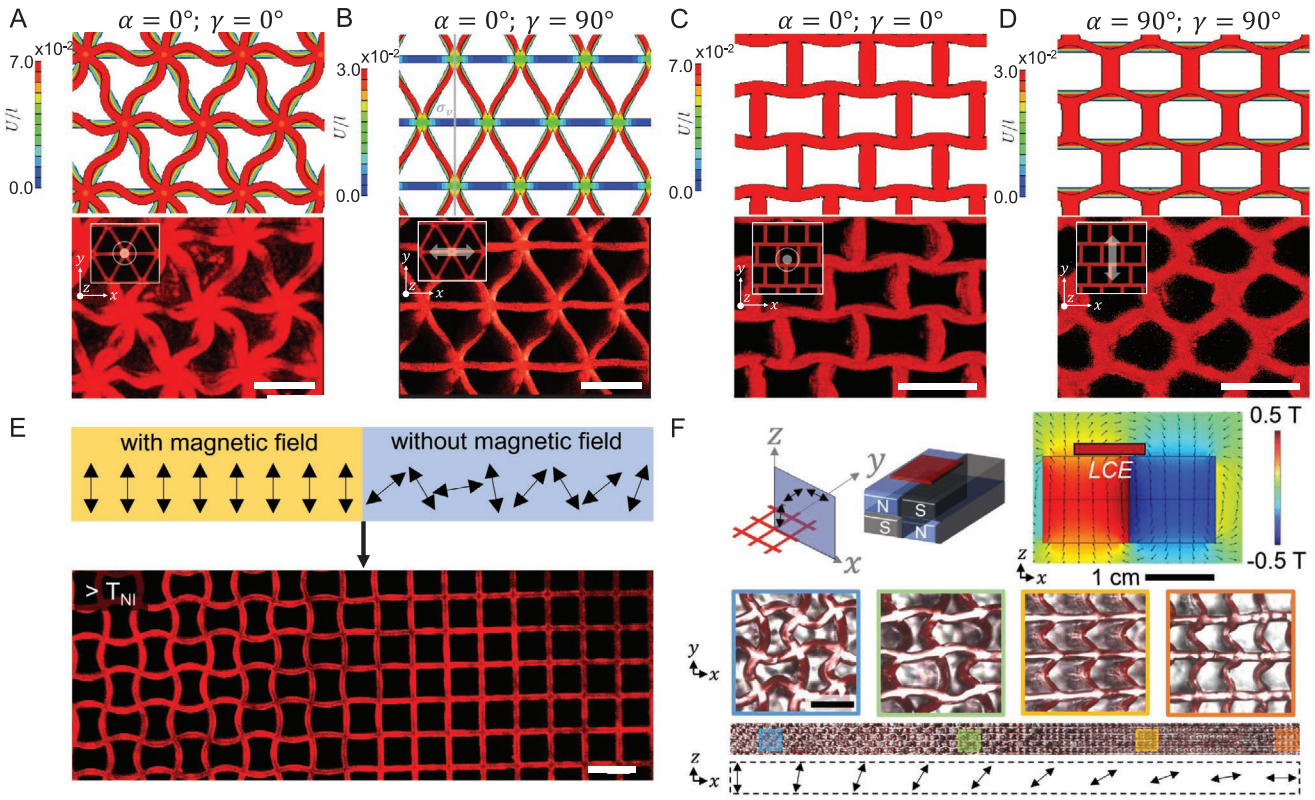

Figure 3. Introduction of different lattice geometries and area-specific director orientations to LCE microcellular structures. A–D) FE simulations for infinitely large lattices (top) and fluorescence confocal microscopy images (bottom) depicting the deformations of the lattices above T_{NI} for: A) triangular lattice with $l/h = 1.9$ and $h/t = 4.27$ above T_{NI} for the case of mesogenic alignment with $\alpha = 0°$, $\gamma = 0°$; B) triangular lattice with the mesogenic alignment defined by $\alpha = 0°$, $\gamma = 90°$; C) staggered square lattice with $l/h = 0.6$ and $h/t = 6.67$ above T_{NI} for the case of mesogenic alignment with $\alpha = 0°$, $\gamma = 0°$; D) staggered square lattice with mesogenic alignment defined by $\alpha = 90°$, $\gamma = 90°$. The color in FE results corresponds to the normalized magnitude of the displacement field in the isotropic phase (displacement U divided by original lattice length l). Fluorescence confocal microscopy images illustrate the deformations of the microstructures at $T = 135$ °C $> T_{NI}$. The insets in the top left corner of the microscopy images show the structure of the undeformed lattice below T_{NI}. The double-headed gray arrows in the inset illustrate the projection of the 3D mesogenic director in the xy-plane. E) Experimental fluorescence confocal microscopy image of an LCE square lattice strip with $l/h = 0.6$, $h/t = 6.67$, and $h = 100$ µm at $T = 135$ °C $> T_{NI}$. Stepwise polymerization has been used to introduce z-alignment on the left and isotropic alignment on the right. Schematics of the mesogenic director are shown on the top. F) Top: a magnetic field with orientation continuously changing from z-axis to x-axis can be generated by placing two magnets side-by-side with N poles facing upward and downward, respectively. The right plot shows the resulting magnetic field calculated using COMSOL. Bottom: optical microscopy images of an LCE square lattice polymerized in such spatially varying magnetic field. At $T = 135$ °C $> T_{NI}$ the lattice displays gradually changing, region-specific symmetry breakings along the strip. The double headed arrows in (E) and (F) mark the mesogenic director. Scale bars: A–F) 100 µm.

While so far we have focused on cellular structures with edges connected end-to-end with a center of inversion symmetry i at the nodes, we next consider a staggered brick-wall architecture with $C2mm$ symmetry and edges connected in an end-to-side manner to provide enhanced flexibility at the nodes. This geometry transforms into a re-entrant hexagonal lattice when the nematic director is aligned along the z-axis (i.e., $\alpha = 0°$ and $\gamma = 0°$, Figure 3C) and into a pseudo-hexagonal lattice when the nematic director is along the y-axis (i.e., $\alpha = 90°$ and $\gamma = 90°$, Figure 3D), with $C2mm$ symmetry preserved in both cases. It is important to highlight that these lattice transformations are not triggered by any buckling instabilities, which are prevented by the enhanced flexibility of the nodes. As such, these results indicate that the range of achievable deformations can be further expanded by engineering the nodes to control the lattice connectivity (Figure S16, Supporting Information).

Further, our approach based on magnetic alignment enables us to expand the range of deformations by encoding area-specific mesogenic alignments in the LCEs to ultimately realize spatially varying deformation modes. For example, utilizing stepwise polymerization with a photomask, we can readily prescribe director alignment only to certain regions where anisotropic deformation will take place locally (Figure 3E). Additionally, more control on the local mesogenic alignment can be achieved by applying a spatially varying magnetic field. As an example, a magnetic field with orientation continuously changing from z-axis to x-axis can be generated by placing two magnets side-by-side with N poles facing upward and downward, respectively (Figure 3F; Figures S17 and S18, Supporting Information). Importantly, by applying such a magnetic field during the polymerization process, a gradient of the director orientations along the sample can be encoded. As shown in Figure 3F, when applied to a square lattice, the buckled pattern

with *P4gm* symmetry shown in Figure 2B emerges on the left side in the isotropic phase and the anisotropic buckling pattern with *Pm* symmetry reported in Figure 2D on the right side, whereas in between the deformation seamlessly evolve between these two distinct symmetry states (see Figures S17 and S18, Supporting Information for the results in a triangular lattice).

Having demonstrated that the interplay between molecular and architectural anisotropy in cellular structures gives rise to a wide range of deformations, we now explore the possibility to engineer LCE microcellular surfaces with switchable and direction-dependent properties induced by designed symmetry breakings. Since the high strength/weight ratio of cellular structures makes our surfaces a good candidate for object transportation (note that they can hold objects ≈100× heavier than themselves), we consider a square lattice with different mesogenic alignments and study the effect of the triggered symmetry breakings on its surface frictional properties. In our tests, we heated the LCE samples up to $T = 135$ °C > T_{NI} (a temperature well above T_g), placed a metal ball (diameter 5 mm, weight 0.5 g, ≈100× heavier than the weight of LCE cellular structures underneath) on their surface, slowly tilted the underlying stage and measured the smallest tilting angle, θ_{cr}, for which the metal ball started to roll (see Supporting Information for details). Note that we considered four different sliding directions: two parallel to the σ_{v1} mirror plane (identified by $\eta = 90°$ and 270°) and two parallel to the σ_{v2} mirror plane (identified by $\eta = 0°$ and 180°—see inset in **Figure** 4A). In Figure 4A, we report θ_{cr} measured for the four sliding directions in the case of mesogenic director aligned (i) isotropically, (ii) along the z axis (i.e., $\alpha = 0°$ and $\gamma = 0°$), (iii) in the σ_{v1} mirror plane and tilted 45° from the C_4 axis (i.e., $\alpha = 0°$ and $\gamma = 45°$) and (iv) along the x axis (i.e., $\alpha = 0°$ and $\gamma = 90°$). As expected, in the case of isotropic alignment, θ_{cr} is identical in four considered sliding directions ($\theta_{cr} \approx 2.0°$, see black dot in Figure 4A, left) as the lattice maintains the *P4mm* symmetry upon heating above T_{NI}. Similar isotropic sliding behavior is observed also for $\alpha = 0°$ and $\gamma = 0°$, since the structure retains C_4 rotational symmetry through the N–I phase transition. However, for $\alpha = 0°$

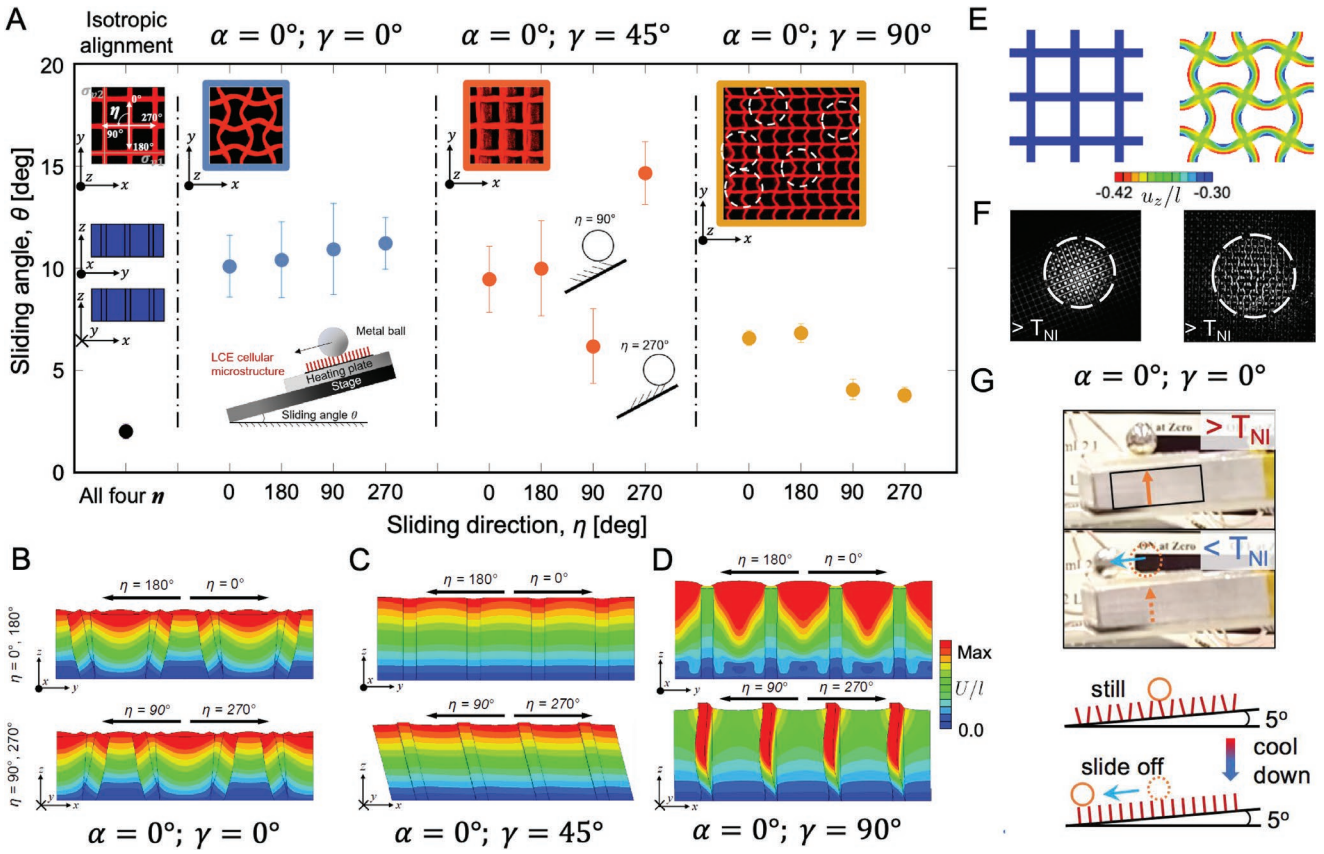

Figure 4. Direction-dependent and switchable frictional properties. A) Sliding angles of metal balls, θ_{cr}, along four orthogonal directions of an LCE square microcellular structures with $l/h = 0.6$ and $h/t = 6.67$ at $T = 135$°C >T_{NI} for isotropic alignment and mesogenic director defined by (α, γ) = (0°, 0°), (0°, 45°) and (0°, 90°). Insets show the fluorescence microscopy data for the corresponding symmetry breaking of the LCE microlattices and the experimental setup and anisotropy in wall orientation. Note that buckling of the walls in the case of (α, γ) = (0°, 90°) occurs in both right and left directions, as depicted by the circled regions in the microscopy image. B–D) FE snapshots showing side views (in both the *yz*- and *xz*-planes) of square lattices in the isotropic phase with mesogenic director defined by B) (α, γ) = (0°, 0°); C) (0°, 45°), and D) (0°, 90°). Color denotes the normalized amplitude of the displacement field. E) FE snapshots showing top views of square lattices in the isotropic phase for isotropic alignment and mesogenic director defined by (α, γ) = (0°, 0°). Color denotes the normalized amplitude of the displacement along the *z* direction. F) Microscopy images illustrating the contact area between the metal ball and the LCE cellular surface in the isotropic phase for isotropic alignment and mesogenic director defined by (α, γ) = (0°, 0°). G) For a square lattice with $\alpha = 0°$ and $\gamma = 0°$, a metal ball remains still for $T > T_{NI}$ and roll for $T < T_{NI}$ when $\theta = 5°$.

and $\gamma = 0°$, θ_{cr} is substantially larger than the one found for the isotropic lattice (i.e., 10.5° vs 2.0°), despite the similar elastic modulus of the two structures at high temperature. We attribute such difference to the non-planar features induced by buckling of the surface of the structure (Figure 4E) as well as a slight increase of the contact area between LCE and the metal ball (Figure 4F) for $\alpha = 0°$ and $\gamma = 0°$.

Differently, in the case of (α, γ)=(0, 45°) and (0, 90°), θ_{cr} shows a pronounced direction-dependence, which is consistent with the *Pm* symmetry exhibited by these lattices in the isotropic phase. More specifically, in the case of $\alpha = 0°$ and $\gamma = 45°$, we find that $\theta_{cr} \approx 10.0°$ for $\eta = 0°$ and 180°, whereas $\theta_{cr} \approx 6.0°$ and ≈15.0° for $\eta = 90°$ and 270°, respectively, with the difference in θ_{cr} measured for $\eta = 90°$ and 270° caused by the sheared plates that facilitate the rolling along the shearing direction ($\eta = 90°$), but provide additional resistance for rolling in the opposite direction ($\eta = 270°$; see insets in Figure 4A and Figure 4C). Further, for $\alpha = 0°$ and $\gamma = 90°$, we find that $\theta_{cr} \approx 5.5°$ for $\eta = 0°, 180°$ and $\theta_{cr} \approx 4.0°$ for $\eta = 90°, 270°$. Although this mesogenic alignment also leads to a pattern with *Pm* symmetry in the isotropic LC phase, as suggested in Figure 2D, the lack of anisotropy along the *x*-axis caused by the buckling both leftwards and rightwards can introduce domain-like patterns (see rightmost inset in Figure 4A) and thus eliminating the difference between θ_{cr} for $\eta = 90°$ and 270°. Moreover, we want to point out that the observed behaviors are robust, as the deterioration of the lattices upon multiple cycles of actuation is minimal (Figure S19, Supporting Information) and that the presence of metal ball does not affect the deformation behaviors of LCE structures (Figure S20, Supporting Information).

Remarkably, our platform not only allows for direction-dependent frictional properties, but also provides means to change these properties by programming the temperature. For example, since for a square lattice with $\alpha = 0°$ and $\gamma = 0°$, $\theta_{cr} \approx 2°$ and ≈10° at $T = 115$ °C and $T = 135$ °C, respectively, we expect the metal ball to remain still for $T > T_{NI}$ and roll for $T < T_{NI}$ when $\theta \in [2°, 10°]$. The experimental results reported in Figure 4G for $\theta = 5°$ at $T = 135$ °C (above T_{NI} and T_g) and 115 °C (below T_{NI} and above T_g) confirm our hypothesis and demonstrate that the sliding of the metal ball can be dynamically controlled by simply changing the temperature (see also Movie S3, Supporting Information). These results suggest the potential of our platform to dynamically control the adhesion force and movement on the objects sitting above.

The results of Figure 4 suggest that the designed symmetry breakings not only affect the direction-dependent frictional properties of the LCEs microcellular surfaces in the static regime, but also in the dynamic one, opening avenues for a new range of applications, such as locomotion and objects transport. To further demonstrate this point, we harness our capability to encode customizable area-specific director alignment to realize selective object transport. In particular, we consider a square lattice polymerized in a spatially varying magnetic field similar to the one shown in Figure 3F, so that the mesogen director gradually changes from $\gamma = 70°$ to 110°, while keeping $\alpha = 0°$. Such spatially varying nematic alignment induces the lattice walls to tilt towards the sample center upon thermal actuation (see schematics in **Figure 5**A and Figure S19C, Supporting Information). As such, while for $T = 110$ °C $< T_{NI}$, in full

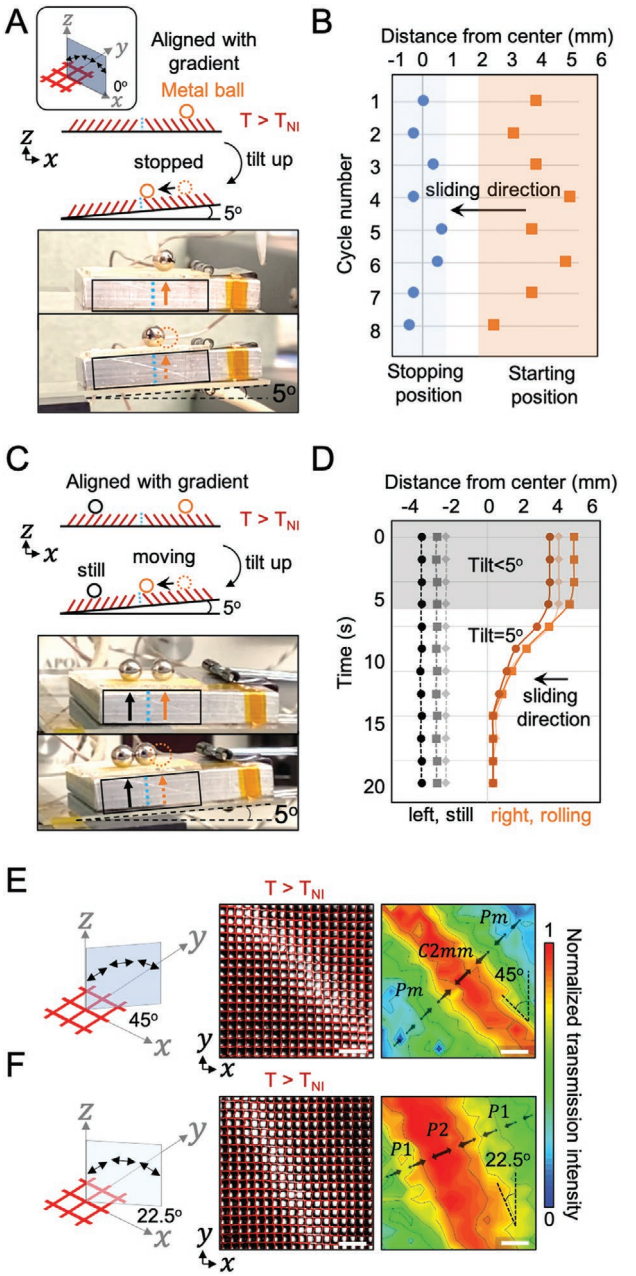

Figure 5. Area-specific symmetry breakings and so-induced material functions. A,B) Controlled object transport for a square lattice with mesogenic director gradually changing from $\gamma = 70°$ to 110°, while keeping $\alpha = 0°$. A) At $T = 135°C > T_{NI}$, a metal ball stops in the middle of the lattice when tilted by 5°. B) Starting and stopping positions of the metal ball recorded during 8 tests. C,D) Selective object transport for a square lattice with mesogenic director gradually changing from $\gamma = 70°$ to 110°, while keeping $\alpha = 0°$. C) When the lattice is tilted by 5° only the ball on the right side moves as it is characterized by a lower coefficient of friction. D) Trajectories of three pairs of metal balls initially placed at opposite ends of the samples, followed by a tilting to 5°. E,F) Optical microscopy images and transmitted light intensity profile at $T = 135$ °C $> T_{NI}$ by an LCE square lattice with mesogenic director gradually changing from $\gamma = 70°$ to 110°, while keeping $\alpha = 45°$ (E) or $\alpha = 22.5°$ (F). Double-headed black arrows in the right plots of (E) and (F) denote the projection of the 3D mesogenic director field in the *xy*-plane. Scale bars: 200 µm.

agreement with the results on Figure 4A, a metal ball placed on the LCE lattice slides off at $\theta_{cr} \approx 2°$, when the temperature is increased to $T = 135$ °C $> T_{NI}$ the ball not only starts sliding at $\theta_{cr} \approx 5°$ (as predicted by the results reported in Figure 4A), but also stops in the middle of the strip, where the shearing direction of the lattices changes abruptly leading to a higher frictional coefficient (Movie S3, Supporting Information). Note that the point of arrest does not dependent on the starting positions of the metal ball, confirming the robustness of the controlled object transport (Figure 5B). Finally, our patterned microcellular surface also enables selective object transport. When two identical metal balls were placed on two ends of the sample and the stage was tilted to 5°, only the metal ball on the right side moves and stops at the center, whereas the metal ball on the other side remains still (Figure 5C and Movie S3, Supporting Information). Figure 5D shows the trajectories of three pairs of metal balls and further confirms the robustness of the selectivity over the motion of cargoes placed at different areas of the patterned film. These unique results demonstrate that the combination of transport region control and selective object movement enabled by patterning mechanical deformations and symmetry breakings in LCE cellular structures may lead to applications in the manipulation of object transport on structural surfaces.

The macroscopic patterning of molecular alignment also provides opportunities to realize tunable, area-specific optical modulation. To exemplify this idea, we fabricated an LCE square lattice with mesogenic director gradually changing from $\gamma = 70°$ to 110°, while keeping $\alpha = 45°$ (Figure 5E). As expected, in the nematic phase the lattice transmits light with spatially uniform intensity under optical microscope (Figures S21 and S22, Supporting Information). However, when heated above T_{NI}, the deformed lattice modulates the transmitted light intensity (Figures 5E—middle and right columns, and Figure S22, Supporting Information). In particular, dark-bright-dark regions emerge corresponding to the *Pm-C2mm-Pm* change of the local symmetry breakings. Moreover, the distribution of transmitted light can be controlled by manipulating the applied magnetic field to vary the nematic directors. As shown in Figure 5F, by changing α from 45° to 22.5° (while keeping the same spatially varying γ), we can re-orient the light band in the isotropic phase at an angle of 22.5° with respect to the vertical direction.

3. Conclusion

We have shown that magnetic field-aligned LCEs provide an excellent platform to program molecular and architectural anisotropy independently and realize reconfigurable cellular structures that exhibit a wide range of temperature-dependent deformation modes, including isotropic/anisotropic buckling, chiral/achiral buckling, tilting, twisting and shearing. These symmetry breakings can be exploited in materials with direction-dependent frictional properties. Furthermore, the unique capabilities of magnetic alignment enables us to encode area-specific molecular anisotropies and the associated localized deformation patterns, of which we showcased potential applications of cellular materials in dynamic light intensity modulation and on-surface object transport. We believe our work not only unveils general and fundamental materials design principles to further enrich the achievable symmetry breakings and resulting non-trivial deformation modes of cellular structures, but also lays the foundation for the design of the next generation of metamaterials with programmable dynamic direction-dependent properties. Finally, we envision that material fabrication by magnetic alignment can be further combined with other strategies to control the mesogenic director, such as photoalignment and 3D printing, to realize core–shell structures with surface and bulk regions that can be programmed independently.

Supporting Information

Supporting Information is available from the Wiley Online Library or from the author.

Acknowledgements

This work was supported by the National Science Foundation (NSF) through the Designing Materials to Revolutionize and Engineer our Future (DMREF) program under Award No. DMR-1922321 and the Harvard University Materials Research Science and Engineering Center (MRSEC) under Award No. DMR-2011754. K.B. also acknowledges support from the Simons Collaboration on Extreme Wave Phenomena Based on Symmetries. Microfabrication and scanning electron microscopy were performed at the Center for Nanoscale Systems (CNS) at Harvard, a member of the National Nanotechnology Coordinated Infrastructure Network (NNCI), which is supported by the NSF under NSF ECCS Award No. 1541959. The authors would like to thank Bolei Deng, Dr. Michael M. Lerch, Anqi Chen, Dr. Mikhail Zhernenkov, and Dr. Guillaume Freychet for fruitful discussions and experimental help.

Conflict of Interest

The authors declare no conflict of interest.

Author Contributions

S.L., G.L., and Y.Y. contributed equally to this work. S.L., G.L., Y.Y., J.A., and K.B. conceived the idea and designed the study. G.L. performed the finite element simulations. S.L., Y.Y., A.R., and A.S.Y. performed the experiments. S.L., G.L., Y.Y., J.A., and K.B. analyzed the results and wrote the manuscript with inputs from all authors. J.A., and K.B. supervised the project.

Data Availability Statement

The data that support the findings of this study are openly available at https://github.com/glibrandi/Liquid-Crystal-Elastomers.git.

Keywords

cellular microstructures, liquid crystalline elastomers, symmetry breakings

Received: June 30, 2021
Published online:

[1] L. J. Gibson, M. F. Ashby, in *Cellular solids: Structure and Properties*, 2nd ed., Cambridge Solid State Science Series, Cambridge University Press, Cambridge, UK **1997**, pp. i–vi.
[2] R. S. Lakes, *Annu. Rev. Mater. Res.* **2017**, *47*, 63.
[3] J. Liu, T. Gu, S. Shan, S. H. Kang, J. Weaver, K. Bertoldi, *Adv. Mater.* **2016**.
[4] J. Valentine, S. Zhang, T. Zentgraf, E. Ulin-Avila, D. A. Genov, G. Bartal, X. Zhang, *Nature* **2008**, *455*, 376.
[5] H. He, C. Qiu, L. Ye, X. Cai, X. Fan, M. Ke, F. Zhang, Z. Liu, *Nature* **2018**, *560*, 61.
[6] J. Bauer, S. Hengsbach, I. Tesari, R. Schwaiger, O. Kraft, *Proc. Natl. Acad. Sci. USA* **2014**, *111*, 2453.
[7] Z. Hu, K. V. Thiyagarajan, A. Bhusal, T. Letcher, Q. Fan, Q. Liu, D. Salem, *Compos. B Eng.* **2017**, *121*, 108.
[8] J. Summers, *Mater. Des.* **2011**, *32*, 512.
[9] T. A. Schaedler, A. J. Jacobsen, A. Torrents, A. E. Sorensen, J. Lian, J. R. Greer, L. Valdevit, W. B. Carter, *Science* **2011**, *334*, 962.
[10] J.-H. Lee, L. Wang, M. C. Boyce, E. L. Thomas, *Nano Lett.* **2012**, *12*, 4392, pMID: 22783965.
[11] X. Xia, A. Afshar, H. Yang, C. Portela, D. Kochmann, C. Leo, J. Greer, *Nature* **2019**, *573*, 205.
[12] J. W. Boley, W. M. van Rees, C. Lissandrello, M. N. Horenstein, R. L. Truby, A. Kotikian, J. A. Lewis, L. Mahadevan, *Proc. Natl. Acad. Sci. USA* **2019**, *116*, 20856.
[13] S. H. Kang, S. Shan, W. L. Noorduin, M. Khan, J. Aizenberg, K. Bertoldi, *Adv. Mater.* **2013**, *25*, 3380.
[14] Y. Kim, H. Yuk, R. Zhao, S. Chester, X. Zhao, *Nature* **2018**, *558*, 274.
[15] X. Zhu, Y. Zhang, D. Chandra, S.-C. Cheng, J. M. Kikkawa, S. Yang, *Appl. Phys. Lett.* **2008**, *93*, 161911.
[16] N. Li, E. Xu, Z. Liu, X. Wang, L. Liu, *Sci. Rep.* **2016**, *6*, 1.
[17] N. Anantharaju, M. V. Panchagnula, S. Vedantam, S. Neti, S. Tatic-Lucic, *Langmuir* **2007**, *23*, 11673.
[18] J. Shim, P. Wang, K. Bertoldi, *Int. J. Solids Struct.* **2015**, *58*, 52.
[19] T. J. White, D. J. Broer, *Nature Mater.* **2015**, *14*, 1087.
[20] C. Ohm, M. Brehmer, R. Zentel, *Adv. Mater.* **2010**, *22*, 3366.
[21] M. Yamada, M. Kondo, J.-i. Mamiya, Y. Yu, M. Kinoshita, C. J. Barrett, T. Ikeda, *Angew. Chem., Int. Ed.* **2008**, *47*, 4986.
[22] K. Urayama, S. Honda, T. Takigawa, *Macromolecules* **2006**, *39*, 1943.
[23] A. Kaiser, M. Winkler, S. Krause, H. Finkelmann, A. M. Schmidt, *J. Mater. Chem.* **2009**, *19*, 538.
[24] J. Shin, M. Kang, T. Tsai, C. Leal, P. V. Braun, D. G. Cahill, *ACS Macro Lett.* **2016**, *5*, 955.
[25] T. H. Ware, M. E. McConney, J. J. Wie, V. P. Tondiglia, T. J. White, *Science* **2015**, *347*, 982.
[26] J.-a. Lv, Y. Liu, J. Wei, E. Chen, L. Qin, Y. Yu, *Nature* **2016**, *537*, 179.
[27] H. Aharoni, Y. Xia, X. Zhang, R. D. Kamien, S. Yang, *Proc. Natl. Acad. Sci. USA* **2018**, *115*, 7206.
[28] Y. Guo, H. Shahsavan, M. Sitti, *Adv. Mater.* **2020**, *32*, 2002753.
[29] J. Küpfer, H. Finkelmann, *Die Makromol. Chem., Rapid Communi.* **1991**, *12*, 717.
[30] A. Kotikian, R. L. Truby, J. W. Boley, T. J. White, J. A. Lewis, *Adv. Mater.* **2018**, *30*, 1706164.
[31] M. López-Valdeolivas, D. Liu, D. J. Broer, C. Sánchez-Somolinos, *Macromol. Rapid Commun.* **2018**, *39*, 1700710.
[32] A. Buguin, M.-H. Li, P. Silberzan, B. Ladoux, P. Keller, *J. Am. Chem. Soc.* **2006**, *128*, 1088.
[33] Y. Yao, J. T. Waters, A. V. Shneidman, J. Cui, X. Wang, N. K. Mandsberg, S. Li, A. C. Balazs, J. Aizenberg, *Proc. Natl. Acad. Sci. USA* **2018**, *115*, 12950.
[34] P.-G. De Gennes, J. Prost, *The Physics of Liquid Crystals*, vol. *83*, Oxford University Press, Oxford, UK **1993**.
[35] M. T. Sims, L. C. Abbott, R. M. Richardson, J. W. Goodby, J. N. Moore, *Liq. Cryst.* **2019**, *46*, 11.
[36] Z. L. Wu, A. Buguin, H. Yang, J.-M. Taulemesse, N. Le Moigne, A. Bergeret, X. Wang, P. Keller, *Adv. Funct. Mater.* **2013**, *23*, 3070.
[37] A. H. Gelebart, D. J. Mulder, M. Varga, A. Konya, G. Vantomme, E. W. Meijer, R. L. B. Selinger, D. J. Broer, *Nature* **2017**, *546*, 632.
[38] D. L. Thomsen, P. Keller, J. Naciri, R. Pink, H. Jeon, D. Shenoy, B. R. Ratna, *Macromolecules* **2001**, *34*, 5868.
[39] P. H. Butler, *Point Group Symmetry Applications: Methods and Tables*, Springer Science & Business Media, New York **2012**.

ADVANCED MATERIALS

Supporting Information

for *Adv. Mater.,* DOI: 10.1002/adma.202105024

Controlling Liquid Crystal Orientations for Programmable Anisotropic Transformations in Cellular Microstructures

Shucong Li, Gabriele Librandi, Yuxing Yao, Austin J. Richard, Alyssha Schneider-Yamamura, Joanna Aizenberg, and Katia Bertoldi**

Supplementary Information for *Controlling Liquid Crystal Orientations for Programmable Anisotropic Transformations in Cellular Microstructures*

Shucong Li[†,a], Gabriele Librandi[†,b], Yuxing Yao[†,a], Austin Richard[b], Alyssha Schneider-Yamamura[b], Joanna Aizenberg [a,b,*], and Katia Bertoldi [b,*]

[a]Department of Chemistry and Chemical Biology,
Harvard University, Cambridge, Massachusetts 02138, USA
[b]Harvard John A. Paulson School of Engineering and Applied Sciences,
Harvard University, Cambridge, Massachusetts 02138, USA
[†]The authors S.L., G.L. and Y.Y. made equal contribution to the work.
[*]To whom correspondence should be addressed; E-mail: bertoldi@seas.harvard.edu, jaiz@seas.harvard.edu

This Supplementary Information document includes: Materials and Methods

Supplemental Results

Figures. S1 to S22

Captions for Supplementary Movies S1 to S3

Other Supplementary Material for this manuscript includes the following:

Movies S1 to S3 (.mp4)

Contents

S1 Materials and Fabrication

S1.1 Materials

The LC monomer **1** 4-(6-Acryloxy-hex-1-yl-oxy)phenyl 4-(hexyloxy)benzoate used for the liquid crystalline elastomers (LCEs) was synthesized following a previously reported procedure by Ratna and co-workers [1]. For the synthesis, 2,5-dihydroxybenzoic acid, benzyl bromide, 4-butyloxybenzoic acid, 4-hydroxybutyl acrylate, N,N-dicyclohexylcarbodiimide (DCC), sodium bicarbonate (NaHCO3), palladium on carbon (10 wt%, matrix activated), 4-pyrrolidinopyridine, Silica gel (Davisil Grade 633, high-purity grade, pore size 60 Å, 200-425 mesh particle size), glacial acetic acid, dichloromethane, and ethanol were purchased from Sigma-Aldrich.

Crosslinker **2**, 1,6-Hexanediol diacrylate (HDDA) was purchased from Sigma-Aldrich, and the inhibitor was removed prior to use. Photoinitiator Darocur® 1173 (bis(2,4,6-trimethylbenzoyl)-phenylphosphineoxide) was purchased from Sigma-Aldrich and used without further purification. Fluorescence label methacryloxyethyl thiocarbamoyl rhodamine B dye for confocal microscopy was purchased from Polysciences, Inc.

For magnetic alignment of the liquid crystal molecules, the high-temperature neodymium magnets (NdFeB, Grade N42SH; 1inch$\times$1/2inch$\times$1/2inch; BX088SH) were purchased from KJ Magnetics, Inc.

For the photolithography and molding, 4-inch Silicon wafers and 6-inch silicon-dioxide carriers were purchased from Nova Electronic Materials. Photoresist SPR220-7.0 was purchased from Microchem. Sylgard® 184 silicone kit was purchased from Ellsworth Adhesive Systems and used as 10:1 (Sylgard® base to curing agent). Microscopy glass slides (25$\times$75 mm, 1 mm in thickness) were obtained from VWR.

S1.2 Experimental methods for fabrication

UV-polymerization was conducted with a Dymax Model 2000 Flood UV Curing System chamber (light intensity of ∼18 mW/cm2) with a custom-made steel-mesh (as neutral density filter) in a nitrogen atmosphere.

Differential scanning calorimetry (DSC) was performed on a Thermal Analysis (TA) DSC Q200 instrument to analyze the phase behaviors of the LC mixtures and LCEs under a nitrogen atmosphere. The program consisted of three cycles from 5 °C to 130 °C with a 10 °C/min rate for the LC mixtures and three cycles from 5 °C to 200 °C with a 10 °C/min rate for the LCEs.

Scanning electron microscopy (SEM) of the Si master was performed on a Zeiss Supra55VP Field Emission Scanning Electron Microscope (FESEM). The tilted view was taken with the SEM holder tilted 25° on a Zeiss Supra55VP FESEM.

Confocal laser scanning microscopy measurements were performed on a Zeiss LSM 700 instrument with 5× and 10× objectives under bright light channel and 532 nm fluorescence channel. LCE was copolymerized with the dye methacryloxyethyl thiocarbamoyl rhodamine B for fluorescence signal. Time-series and 3D reconstruction were analyzed with the Zeiss ZEN black software.

Fabrication of Si masters All cellular structures with designed geometries used for this study were first fabricated on 4" <100> Si wafers (Nova Electronic Materials) by photolithography followed by reactive ion etching (RIE). Spin-coated photoresist (SPR220-7.0) was patterned by UV exposure (375 nm, 470 mJ/cm^2) under the Heidelberg MLA150 Maskless Aligner. The patterned photoresist later served as the mask for the anisotropic dry etching of the underlying Si wafer using an STS ICP RIE System, to obtain the Si microstructures.

Fabrication of PDMS negative molds To make a negative polydimethylsiloxane (PDMS) mold, the Si master was treated with trichloro(1*H*,1*H*,2*H*,2*H*-perfluorooctyl) silane to render the structure hydrophobic. The PDMS precursor (mixture of Sylgard 184® base and the

crosslinker with the ratio of 10:1 (wt:wt), Ellsworth Adhesive Systems) was applied on top of the Si wafer, degassed and cured at 70 °C for 2 h. Finally, the PDMS was carefully peeled off from the Si wafer and used as a negative mold for the synthesis of LCE microcellular structures.

S1.3 Fabrication and characterization of LCE structures

S1.3.1 LCE synthesis and phase behaviors

The LC monomer **1** used for LCEs was synthesized following a previously reported procedure by Ratna and co-workers [1]. Nuclear Magnetic Resonance (NMR) spectra were measured with a Varian Unity/Inova 500 spectrometer (500 MHz). Chemical shifts for the specific ^{1}H-NMR spectra (Fig. S1) were reported relative to the residual solvent peak (in ppm; $CDCl_3$: H = 7.26) [2]. ^{1}H-NMR (Fig. S1) (500 MHz, $CDCl_3$) (ppm): 1.00 (t, J = 7.4, 2.6 Hz, 6H), 1.46 1.68 (m, 8H), 1.75 1.86 (m, 4H), 3.95 4.09 (m, 6H), 4.20 (t, J = 6.0 Hz, 2H), 5.77 5.82 (m, 1H), 6.03 6.12 (m, 1H), 6.32 6.40 (m, 1H), 6.92 7.02 (m, 4H), 7.26 7.28 (m, 1H), 7.43 7.48 (m, 1H), 7.89 (s, 1H), 8.10 8.19 (m, 4H). ^{1}H-NMR spectral properties matched previously reported values[1].

The LCEs used in this study consist of 90.5 w.t.% of LC monomer **1**, 7.5 w.t.% of crosslinker **2** HDDA, and 2 w.t.% of photoinitiator Darocur® 1173, as shown in Fig. S2. We note that increasing the HDDA crosslinking density will result in a smaller actuation strain and can serve as a further control over the symmetry breakings of the LCE cellular microstructures, as we later demonstrated in Fig. S8. To prepare monomer mixtures for LCEs, 90.5 mg of monomer **1**, 7.5 mg of HDDA crosslinker **2**, 2 mg of Darocur® 1173, and a trace amount of methacryloxyethyl thiocarbamoyl rhodamine B (for fluorescent signal) were dissolved and mixed thoroughly in 1 mL of dichloromethane. The solvent was allowed to slowly evaporate on a clean glass slide in the dark overnight to yield dried LC monomer mixture. The phase behavior of the monomer mixture was characterized by differential scanning calorimetry (DSC, Thermal Analysis (TA)

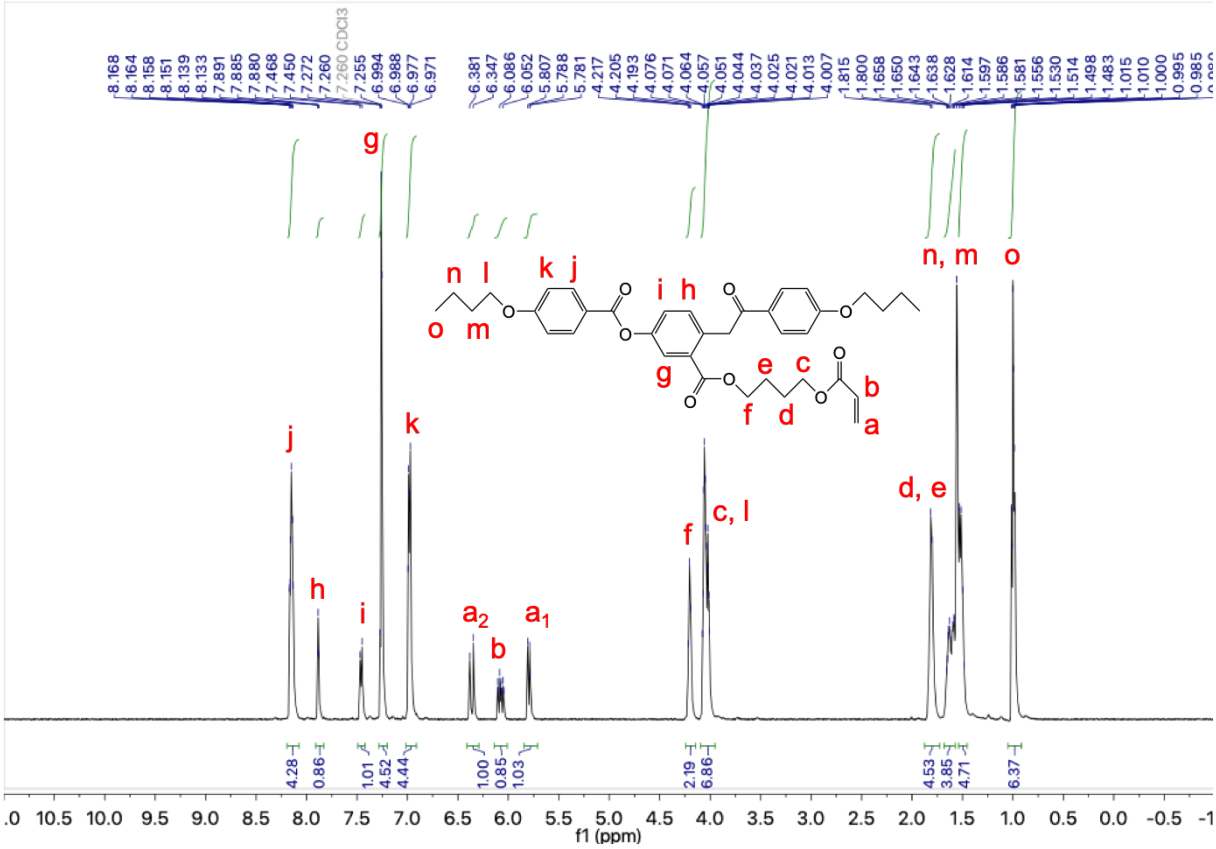

Figure S1: ^{1}H spectrum of the polymerizable LC monomer 4-acryloyloxybutyl 2,5-di(4-butyloxybenzoyloxy) benzoate. We synthesized this molecule following a previously reported procedure [1].

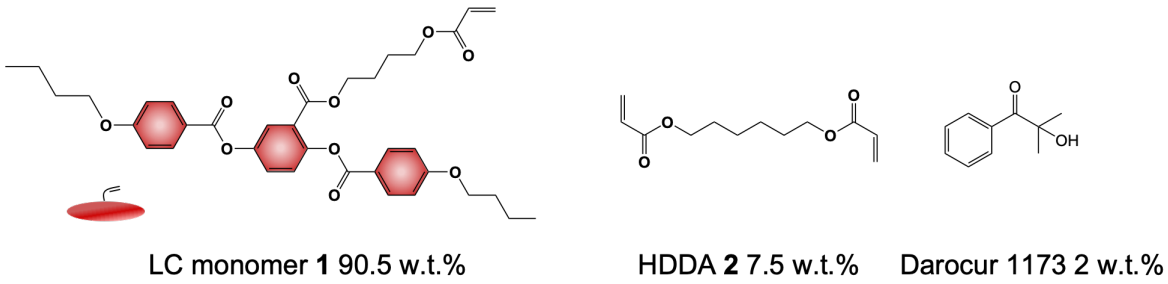

Figure S2: LCE constituents: polymerizable LC monomer, 1,6-hexanediol diacrylate (HDDA) crosslinker, and Darocur® 1173 photoinitiator. These molecules are mixed thoroughly with the weight ratio of: 90.5/7.5/2 before the photo-initiated polymerization.

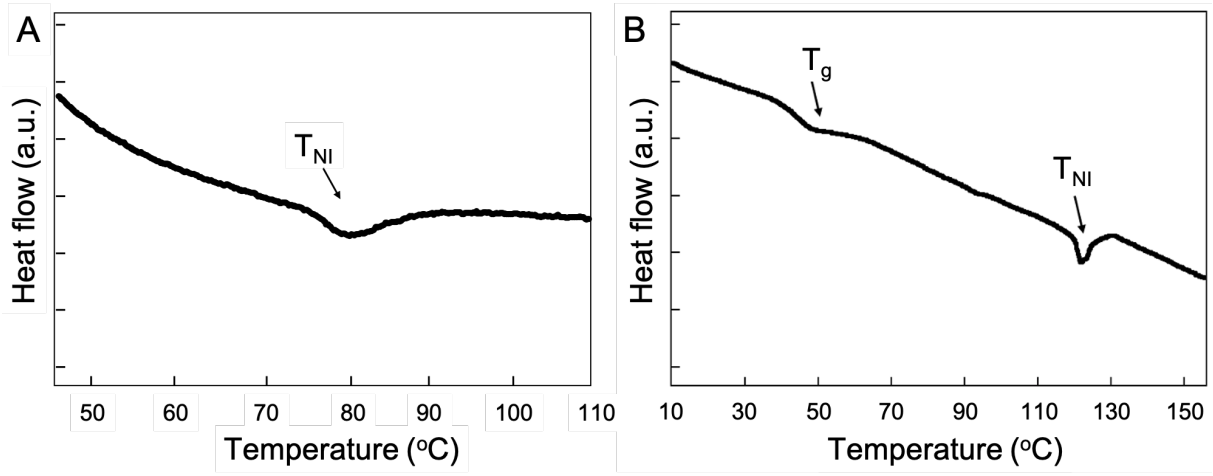

Figure S3: Phase transitions of (A) the LC monomer mixture, and (B) the polymerized LCE as measured using differential scanning calorimetry (DSC) with a 10 °C/min rate. After the polymerization, the LCE shows a sharp peak indicating the T_{NI} at around 125 °C.

DSC Q200). The LC monomer mixture showed a nematic-isotropic phase transition at ∼80 °C, as shown in Fig. S3A. The following polymerization temperature was set at 60 °C to assure a nematic LC phase throughout the curing process for effective magnetic field-induced mesogenic alignment.

The aligned LCE microstructures were fabricated following a previously reported procedure by Aizenberg and coworkers [3]. We applied ∼20 mg of LC monomer mixture into a microstructured PDMS mold and covered it with a glass substrate (25×75 mm, 1 mm in thickness, VWR). As shown in Fig. S4, the sample was placed in a magnetic field generated by the desired assembly of NdFeB-based magnets with a surface field of 0.45 T (NdFeB, Grade N42SH; 1inch×1/2inch×1/2inch; BX088SH, KJ Magnetics, Inc), heated to 90 °C (isotropic phase), cooled down to 60 °C at a rate of 10 °C/min, and exposed to UV (Dymax Model 2000 Flood UV Curing System, light intensity of ∼18 mW/cm^2) in a nitrogen atmosphere to initiate polymerization (note that for isotropically aligned LCE microstructures, we kept the heating plate at 130 °C and directly performed the UV-induced polymerization without any magnets).

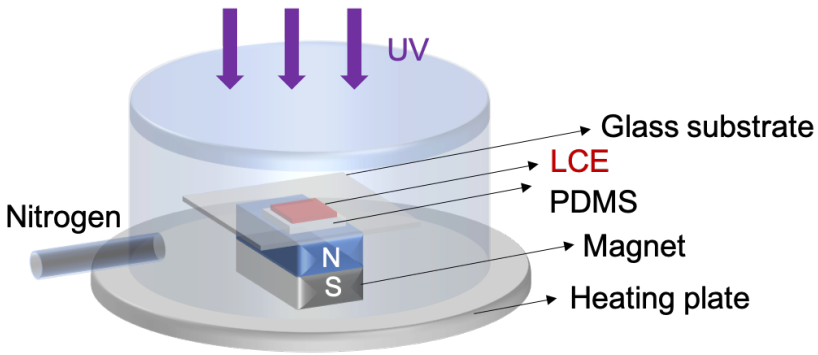

Figure S4: Setup for the synthesis of the LCE microstructures in a designed magnetic field. LC monomer mixture is sandwiched between the PDMS mold and the glass substrate, which is placed on top of the magnets. The temperature of the whole system is controlled by the heating plate underneath. We heat the sample to 90 °C (isotropic phase), cool it down to 60 °C at a rate of 10 °C/min, and exposes it to UV (Dymax Model 2000 Flood UV Curing System, light intensity of ∼18 mW/cm^2) in a nitrogen atmosphere to initiate polymerization. After 30 min of polymerization, the sample is cooled down to room temperature, and the PDMS mold is carefully peeled off to obtain the LCE microstructures.

After 30 min of polymerization, the sample was cooled down to room temperature, and the PDMS mold was carefully peeled off to obtain LCE microcellular structures. The polymerized LCE showed a glass transition temperature (T_g) at 40 °C and a nematic-isotropic (N-I) phase transition at $T_{NI} \sim 125$ °C (Fig. S3B).

S1.3.2 Characterization of the geometries of Si masters

We used Zeiss Supra55VP Field Emission Scanning Electron Microscope (SEM) to characterize 3D microstructures fabricated on Si masters. The tilted-view in Fig. S5A and E were taken with the SEM holder tilted 25°. All geometries of the cellular microstructures fabricated for this study are summarized in Fig. S5 and Table S1.

S1.3.3 Wide angle x-ray scattering (WAXS) and estimations of the scalar order parameter of LCE

To experimentally estimate the initial nematic scalar order parameter, S_0, we conducted

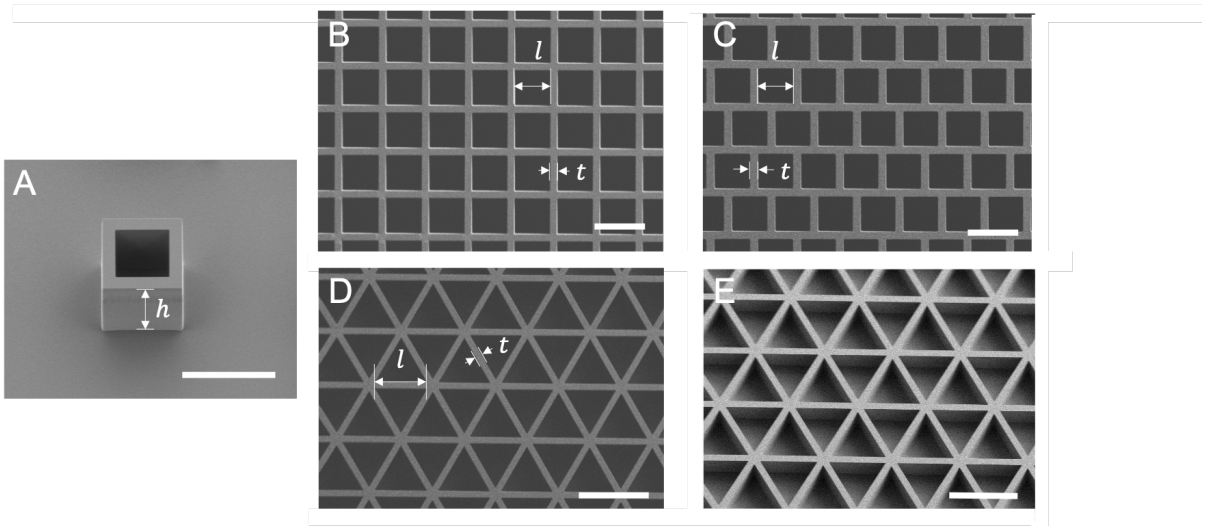

Figure S5: (A) SEM tiled-view image of a square unit. (B-D) SEM top-view images of the Si master with (B) square lattice, (C) staggered square lattice, (D) triangular lattice, and (E) tilted-view of triangular lattice. For the square and staggered square lattices, $l = 60\,\mu$m, $h = 100\,\mu$m and $t = 15\,\mu$m. For the triangular lattice, $l = 90\,\mu$m, $h = 47\,\mu$m and $t = 11\,\mu$m. We later fabricated PDMS stamps with negative structures by polymerizing PDMS precursors on top of these Si masters. LCEs are molded into the desired microcellular structures within PDMS stamps during the polymerization process. Scale bars: $100\,\mu$m.

geometries	inner length l (μm)	height h (μm)	thickness t (μm)
square unit	60	100	15
square lattice	60	100	15
triangular lattice	90	47	11
staggered lattice	60	100	15

Table S1: Dimensions of LCE microcellular structures used in this study.

wide angle x-ray scattering (WAXS) experiments on a block of LCE with height of $\sim$1 mm synthesized in a magnetic field with intensity of 0.45 T. Our WAXS experiments were conducted using an incident x-ray beam with energy of 18.25 keV, size of 40$\times$220 μm and direction perpendicular to the mesogenic alignment of the LCE block (see Fig. S6A). The scattering pattern was collected in transmission mode and recorded on a Pilatus 300 K-W detector of the Soft Matter Interfaces beamline (12-ID SMI) at the National Synchrotron Light Source II (NSLS-II) [4]. As shown in Fig. S6B, we find that at $T = 60$°C the LCE block exhibits a direction-dependent scattering intensity profile with a distinct peak at $q = 1.6$ A^{-1} along the equatorial direction. Such direction-dependent peak corresponds to the distance between neighboring mesogens [5] and indicates that the magnetic field applied during polymerization successfully aligned the mesogens. Further, the initial nematic scalar order parameter, S_0, can be estimated from these WAXS results as [5, 6, 7]:

$$S_0 = \frac{3\left\langle \cos^2\theta \right\rangle - 1}{2} \tag{S1}$$

where $\langle \cos^2\theta \rangle$ is the average cosine square of the angles between the individual mesogens and the global mesogenic director. Here, we estimate the distribution of θ to be the same as the φ indicated in Fig. S6B [5, 6, 7] and calculate $\langle \cos^2\theta \rangle$ as [8]

$$\left\langle \cos^2\theta \right\rangle = \frac{\int_0^{2\pi} I(\varphi)\cos^2\varphi |\sin\varphi|\, d\varphi}{\int_0^{2\pi} I(\varphi)|\sin\varphi|\, d\varphi} \tag{S2}$$

where $I(\varphi)$ denotes the intensity scattered in a direction at an angle φ. Using the angular distributions of the diffracted intensity of the peak shown in Fig. S6D (note that the peak is

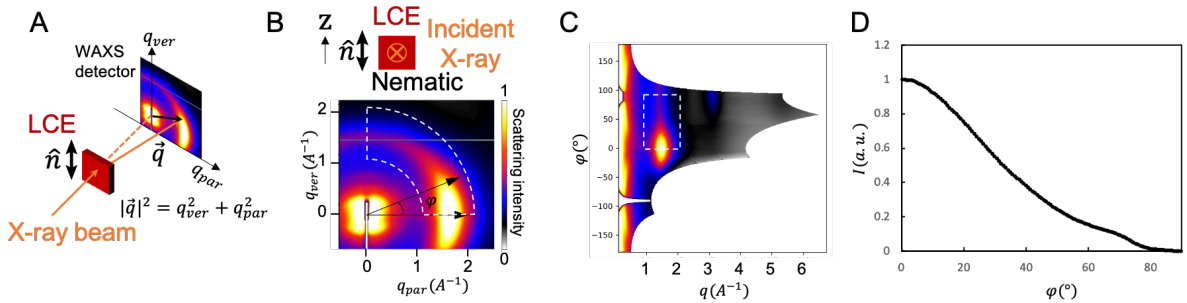

Figure S6: **WAXS measurements for a z-aligned LCE block** (A) Schematic of the WAXS scattering setup. Note that the incident x-ray is perpendicular to the mesogenic director. (B) Two-dimensional WAXS patterns for a z-aligned LCE block. (C) Corresponding transformed intensity profile. (D) Angular distribution of the diffracted intensity of the peak highlighted by a dashed white rectangle in panels B and C with $\varphi \in [0°, 90°]$.

highlighted by a dashed white rectangle in Fig. S6B and C), we obtain $S_0 = 0.21$. As explained in the main text, this value is now used in the constitutive model employed in our Finite Element simulations.

S1.3.4 Confocal characterization of the thermal actuation of LCE cellular structures

To capture the 3D morphology of LCE microstructures at different temperatures, samples were copolymerized with methacryloxyethyl thiocarbamoyl rhodamine B during the synthesis. The samples were monitored with Zeiss LSM 700 confocal optical microscope, with the temperature controlled by a home-made metal heating plate and ambient air cooling. The mechanical reconfigurations of LCE microcellular structures in a temperature cycle between 25 °C and 135 °C are shown in Movie S1 for a large area square lattice and Movie S2 for the square and triangular lattice aligned with different director orientations). It is worth noting the LCEs have a sharp phase transition at around 125 °C and cycling just above and below 125 °C can be readily utilized for fast repeated actuations within seconds. Moreover, the temperature ramping rate does not significantly affect the deformation behaviors of aligned LCE microstructures (Fig. S7).

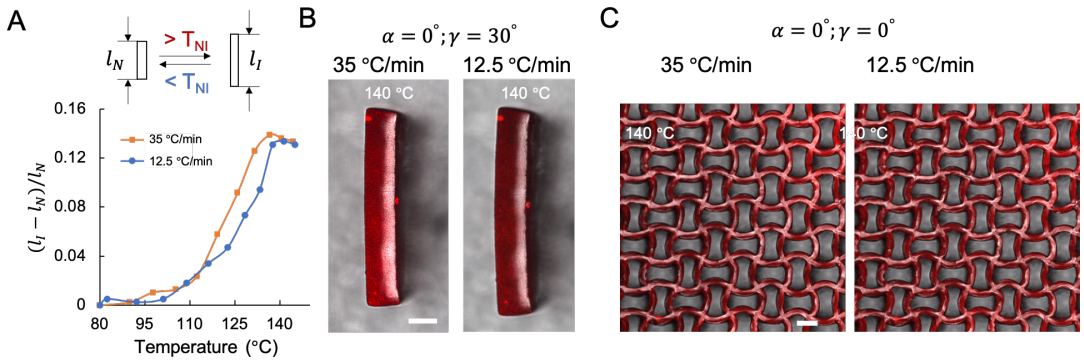

Figure S7: **Dependence of LCE deformations on heating rate.** (A) The elongation strain of a tilt-aligned microplates ($\alpha = 0°$, $\gamma = 45°$) with size 250×50×200 μm (length×width×height) as a function of temperature. l_N and l_I denote the length of LCE microplates in the nematic phase and varying temperature, respectively. (B) Experimental snapshots showing the LCE microplate at $T = 135°\text{C} > T_{NI}$ when heated with rates of 35 °C and 12.5 °C. (C) Experimental snapshots of a LCE square lattice with $\alpha = 0°$ and $\gamma = 0°$ at $T = 135°\text{C} > T_{NI}$ when heated with rates of 35 °C and 12.5 °C. The LCE microstructures have $l/h = 0.6$ and $h/t = 6.67$, where l, h and t denote the length, height and thickness of the plates, respectively. The deforamtion induced by the $N - I$ phase transition in both the isolated plate and the microcellular structure is identical for the two considered heating rates. Scale bars: 50 μm.

S1.3.5 Effect of magnetic field, crosslinking density and temperature ramping rate on the deformation amplitude

The extent of LCE deformation can be tuned by the magnetic field strength during the alignment process (Fig. 1E and (Fig. S8)). With a stronger magnetic field, the extent of shrinkage along the mesogenic director (Fig. 1E) and expansion perpendicular to the mesogenic director through N-I phase transition increase (Fig. S8B). LCE crosslinking density can also affect the deformation behavior: the higher the crosslinking density, the smaller shrinkage along the mesogenic director thought N-I phase transition (Fig. S8C). This effect can also be observed in a LCE cellular surface (Fig. S8D).

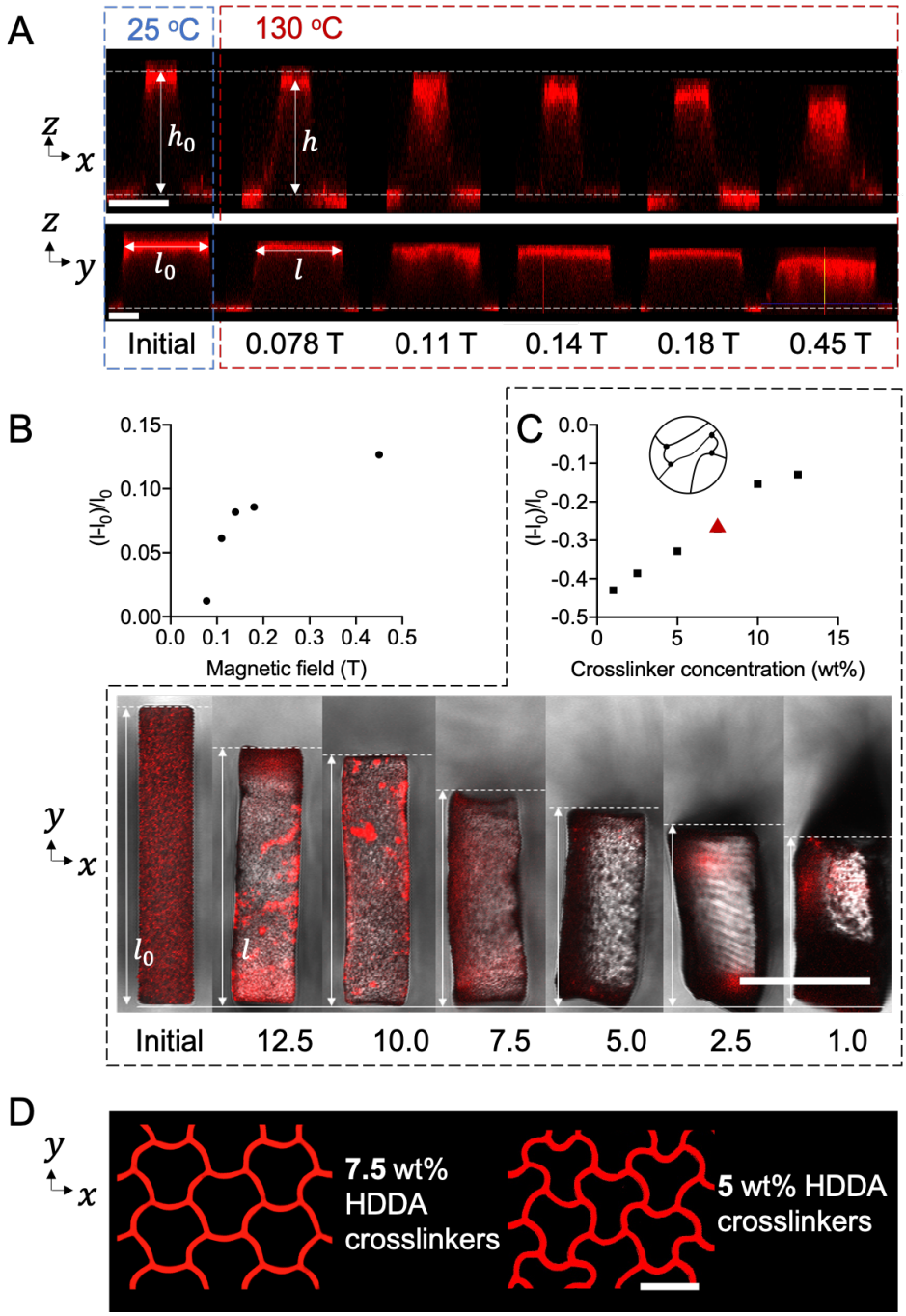

Figure S8: Dependence of LCE deformations on (A,B) applied magnetic field during alignment process and (C,D) crosslinking density. Note that LCE microstructures have mesogenic alignment along the z-axis in (A and D) and along the y-axis in (C).

S1.3.6 Synthesis of LCE cellular structures with aligned and isotropic areas ('on-and-off' patterning)

To encrypt molecular anisotropy to certain regions and leave others isotropic, we used a step-wise polymerization approach (Fig. 3E). The first-step of UV-induced polymerization was carried out with part of the sample covered by a photomask in the absence of a magnetic field at 100 °C (isotropic phase of the reactive mixture) for 10 min in Dymax Model 2000 Flood UV Curing System. This first polymerization locked the LCE in the uncovered area in the isotropic (un-aligned) state (i.e., the right region in Fig. 3E), while left the covered area unpolymerized. Subsequently, we removed the photomask, slowly cooled the system down (at 1 °C/min) to 60 °C (nematic phase of the reactive mixture), and conducted the second polymerization in the presence of the magnetic field. This step encodes the desired mesogenic director to the previously unpolymerized area (i.e., the left region in Fig. 3E). Note that by applying photomasks with specific pattern designs, hierarchical distribution of the isotropic and aligned LCE configurations can be readily written into the cellular structure.

S1.3.7 Synthesis of LCE cellular structures with gradually changing director

To encode more complex area-specific mesogenic alignments in the LCE cellular structures, two block magnets (with the dimensions of 1" × 1/2" × 1/2") were assembled side by side to realize a spatially varying magnetic field (Fig. S17A). The magnetic field generated by the magnet assemblies was calculated in COMSOL Multiphysics with the Magnetic Field Module (Fig. S17B). In the numerical analyses, a magnetic field of 0.5 T is assigned to the surface of magnets and based on this the magnetic field is computed. In Fig. S17B we also report the numerically obtained relationship between the polar angle of the local magnetic field line (which corresponds to the angle γ defining the nematic director) and the distance L from the center of magnets setup in the xz-plane along a line 1 mm above the magnet setup (corresponding to the

thickness of the PDMS mold) in the xz-plane. The result reveals a gradual transition from a x-aligned regime (with $\gamma = 90°$) to a z-aligned regime (with $\gamma = 0°$) through the LCE sample.

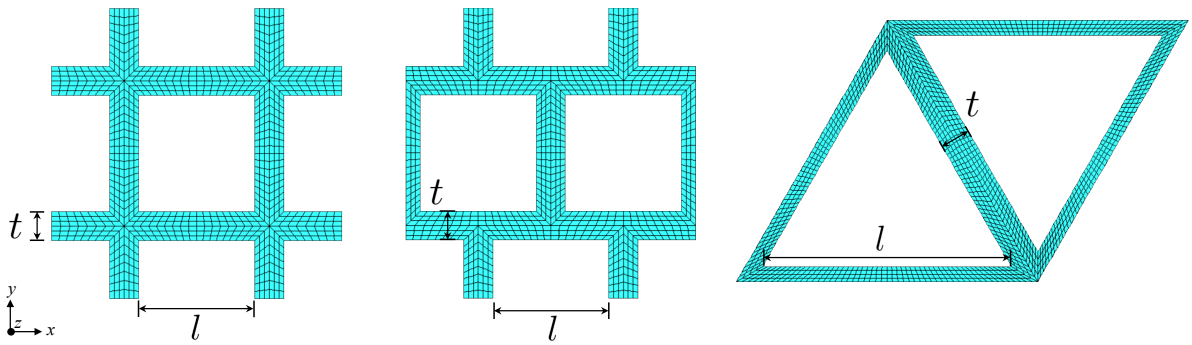

Figure S9: The three super-cells used in FE analyses.

S2 Finite Elements simulations

To get a better understanding of the mechanical behavior of our LCE cellular structures, we conducted Finite Elements (FE) simulations using the commercially available software ABAQUS/Standard. Each mesh was constructed using 8-node brick elements (ABAQUS element type C3D8) and the accuracy was checked by mesh refinement. The response of the LCEs used to fabricate the cellular structures is modeled using the strain energy defined in Eq. (1) of the main text, implemented through an in-house ABAQUS user subroutine (UMAT) (note that the code is provided as Supplementary Materials).

In our FE analysis, we focus on super-cells of three different geometries: square, stagger, and triangle (Fig. S9). In all our simulations, the bottom surface ($i.e.$ z = 0) of the three geometries was modelled to be perfectly bonded to a rigid substrate, while the top surface is free to move. On the lateral surfaces of the super-cells, constraints equations are applied to enforce periodic boundary conditions and mimic the infinite size of the ideal system [9, 10].

We conduct a static analysis (*STATIC step with NLGEOM=ON in Abaqus) and load the structure by linearly decreasing the instantaneous nematic scalar order parameter S^t. For nematic directors that triggers a mechanical instability upon N-I phase transition, we first run an eigenfrequency analysis (*FREQUENCY step in Abaqus) to find the first unstable mode, and

then perturb the original mesh by superimposing the unstable mode. After this preliminary step, the same static analysis previously described is performed.

We also use FE to capture the deformation of the LCE structures that present a gradient in the mesogenic alignment (see S1.3.7). In these cases, our UMAT takes as input the x-coordinates of each element and compute the nematic director orientation based on the local magnetic field orientation. Along the y-direction periodic boundary conditions are applied.

S3 Supplementary Results

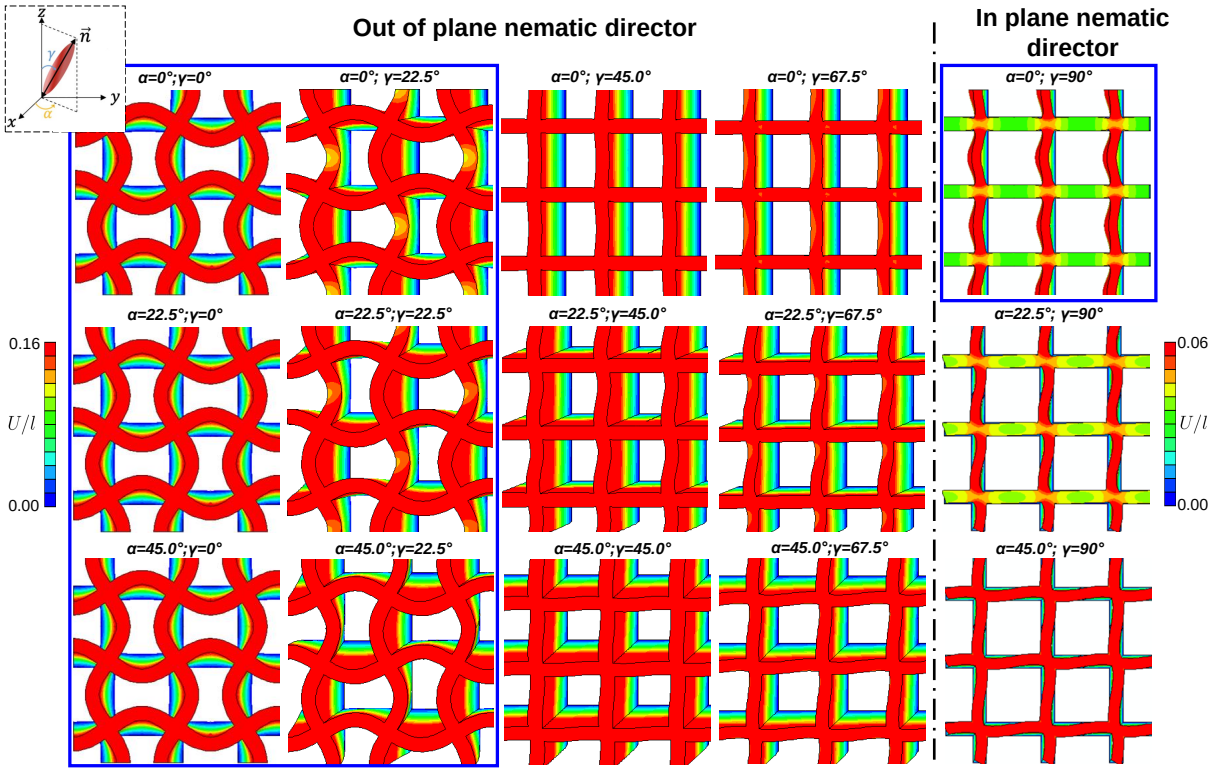

Figure S10: **Numerical results for different mesogenic directors orientation.** FE results for an infinitely large square lattice with $l/h = 0.6$ and $h/t = 6.67$ and different nematic directors upon N-I phase transition. The blue rectangles encompass structures for the N-I phase transition triggers a buckling instability. The color corresponds to the normalized magnitude of the displacement field in the isotropic phase. We find that all the different deformation patterns represent a combination of the four elementary deformation modes described in the main text.

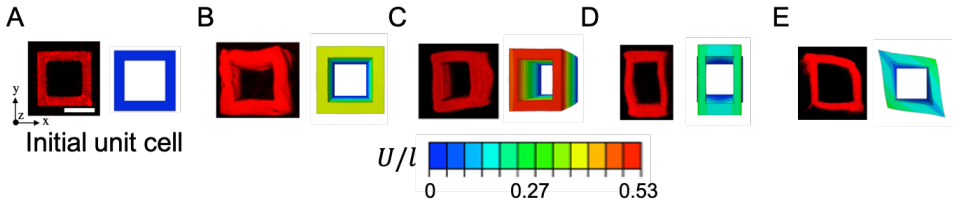

Figure S11: **Response of an isolated square cell.** Fluorescence confocal microscopic images and numerical snapshots of (A) an isolated LCE square unit with $l/h = 0.6$, $h/t = 6.67$ and $h = 100\,\mu$m at $T = 135°$C$> T_{NI}$. We report results for four different mesogenic alignments: (B) $\alpha = 0°$ and $\gamma = 0°$; (C) $\alpha = 0°$ and $\gamma = 45°$; (D) $\alpha = 0°$ and $\gamma = 90°$; (E) $\alpha = 45°$ and $\gamma = 90°$. Scale bar: $50\,\mu$m.

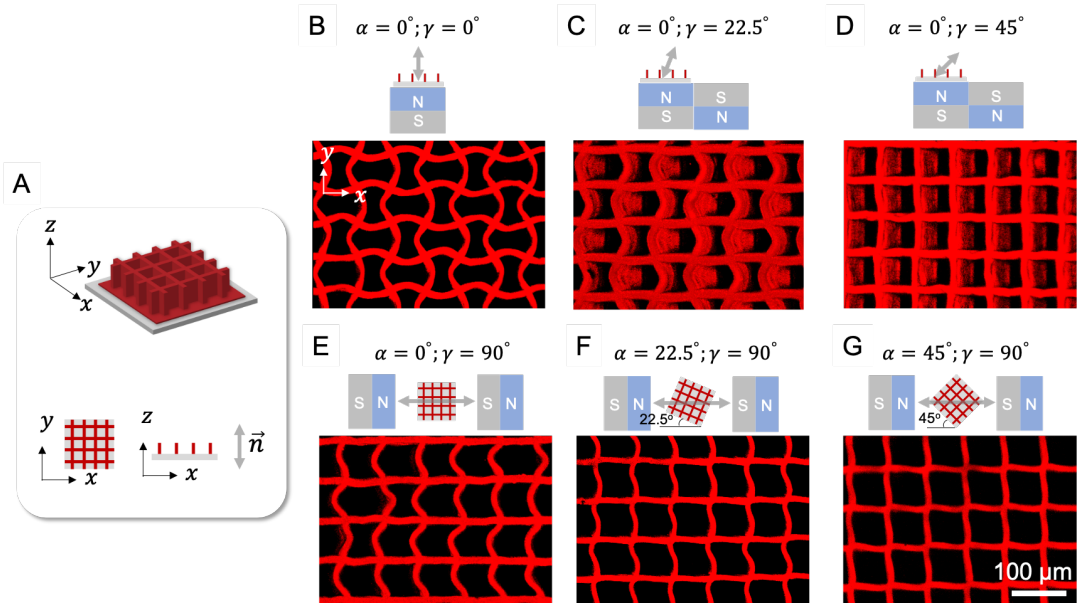

Figure S12: **Characterization of mechanical deformations of square lattices in large area.** Fluorescence confocal microscopic images of LCE square lattices with $l/h = 0.6$, $h/t = 6.67$ and $h = 100\,\mu$m and different mesogenic alignments at $T = 135°$C$> T_{NI}$. Schematics of the magnets arrangement for the desired mesogenic alignment are shown at the top of each image. Scale bars: $100\,\mu$m.

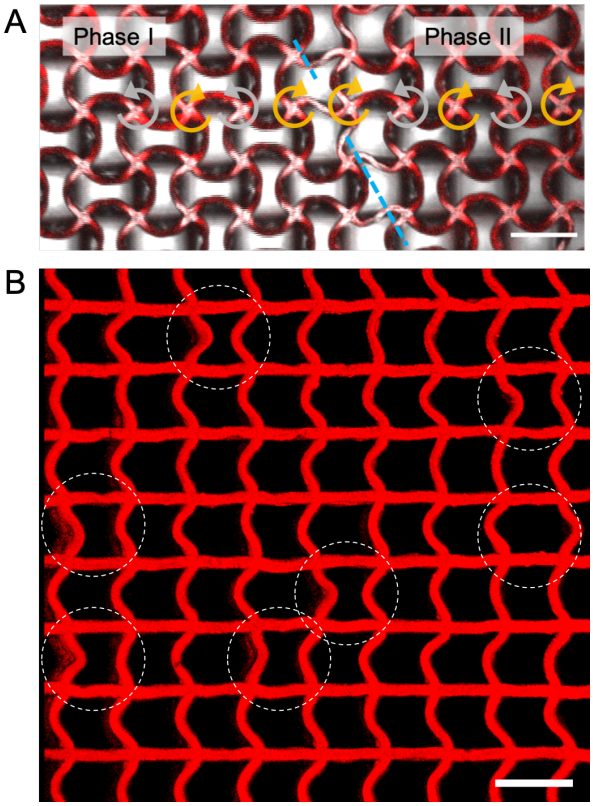

Figure S13: **Domain boundaries.** In our experiments multiple buckling phases emerge triggered by several nucleation events (induced by either by unavoidable geometric imperfections or slight temperature variation throughout the sample). As an example, in (A) we report an LCE square lattice with the mesogenic director oriented along the z-axis. In the figure, the chirality of the nodes is marked with orange (clockwise) or grey (counterclockwise) arrows and the grain boundary is marked with blue dashed lines. Further in (B) we show an x-aligned ($\alpha = 0°$, $\gamma = 90°$) LCE square lattice in which several nucleation events trigger the formation of buckling phases upon the N-I phase transition. Scale bars: $100\,\mu$m

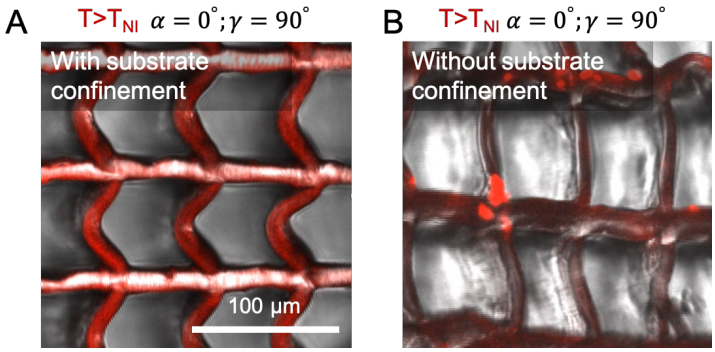

Figure S14: **Effect of the substrate on the deformation behaviors of the LCE cellular microstructures.** To demonstrate the effect of substrate confinement, we fabricated LCE microstructures with and without substrate confinement. Here we show results for a square lattices with $l/h = 0.6$, $h/t = 6.67$ and $l = 60$ μm (where l, h and t denote the length, height and thickness of the plates, respectively) and mesogenic director aligned along the x-axis (i.e. $\alpha = 0°$ and $\gamma = 90°$). (A) The surface-attached LCE structure was obtained by simply synthesizing it on a bare glass slide, as we found that during polymerization a strong bonding forms between the LCE polymer and the glass substrate that provides a very strong interfacial adhesion. We found that in the case of *strong substrate confinement* the expansion of the vertical elements upon N-I phase transition results in their buckling and lead to a deformation pattern identical to that reported in Fig. 2 of the main text. (B) To realize substrate-free LCE microcellular structures, we synthesized them on a glass substrate precoated with a thin layer of polyvinyl alcohol (PVA) (3 w.t.% aqueous solution) that we used as sacrificial layer. The glass-attached LCE structure was then immersed in cold water overnight to dissolve the PVA to release the LCE from the glass substrate. Then the LCE structure was placed on a silicone oil covered glass slide for reduced adhesion during thermal deformation. We found that in the *absence of substrate confinement* the vertical element simply expand and no buckling occurs, leading to a global expansion of the structure in vertical direction.

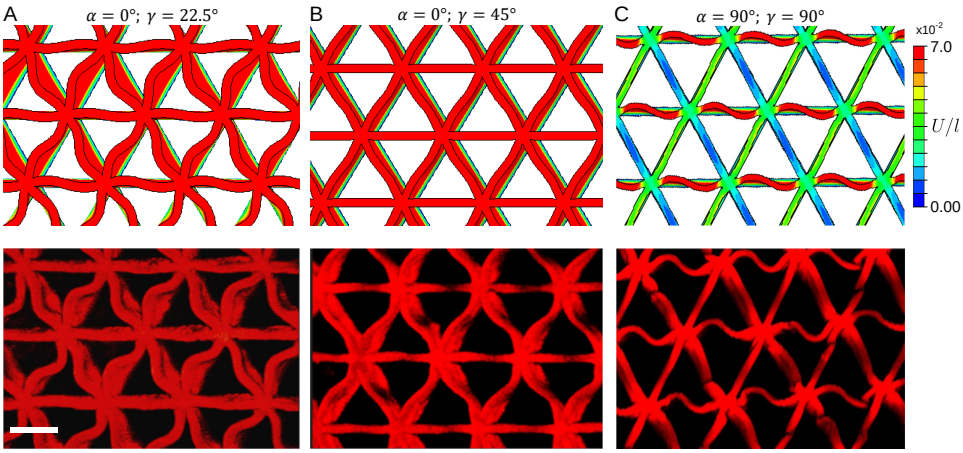

Figure S15: **Symmetry breakings for surface-attached LCE triangular lattice.** Symmetry breakings for surface-attached LCE triangular lattice with $l/h = 1.9$ and $h/t = 4.27$ above T_{NI} for the case of mesogenic alignment defined by (A) $\alpha = 0°$, $\gamma = 22.5°$, (B) $\alpha = 0°$, $\gamma = 45°$ and (C) $\alpha = 90°$, $\gamma = 90°$. Top: FE results for infinitely large lattices upon N-I phase transition. The color corresponds to the normalized magnitude of the displacement field in the isotropic phase. Bottom: fluorescence confocal micrographs illustrating the deformations of the microstructures at $T = 135°\text{C} > T_{NI}$. Scale bars: $100\,\mu$m

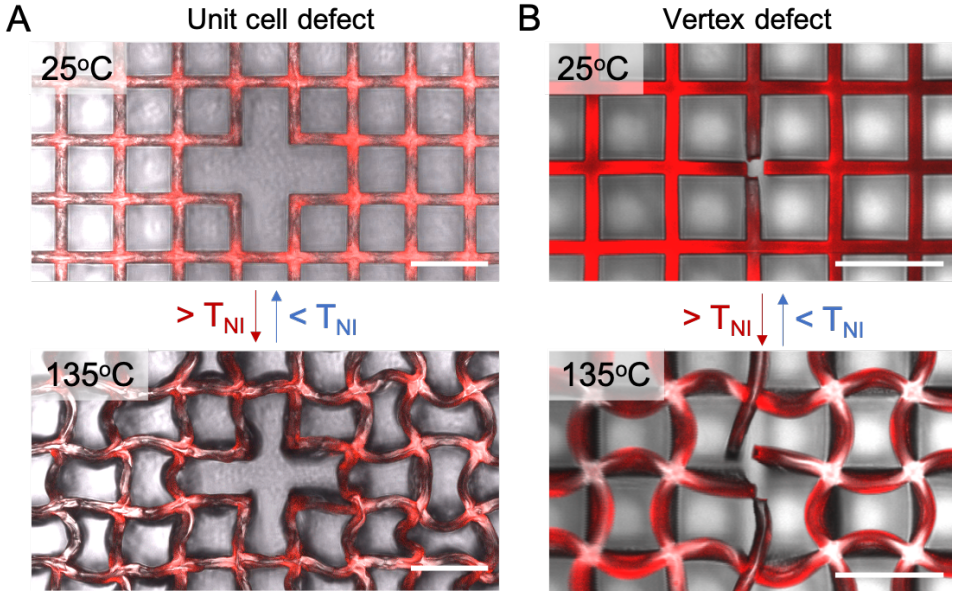

Figure S16: **Effect of intentional defects on lattice reconfigurations.** Lattice reconfigurations triggered upon N-I phase transition in a square lattice with $l/h = 0.6$, $h/t = 6.67$, mesogenic alignment defined by $\alpha = 0°$, $\gamma = 0°$ containing (A) a unit cell defect and (B) a vertex defect. We find that the flexibility introduced by the missing structural elements prevents buckling of the plates adjacent to the defects and further enriches the possible mechanical reconfigurations. Scale bars: $100\,\mu$m

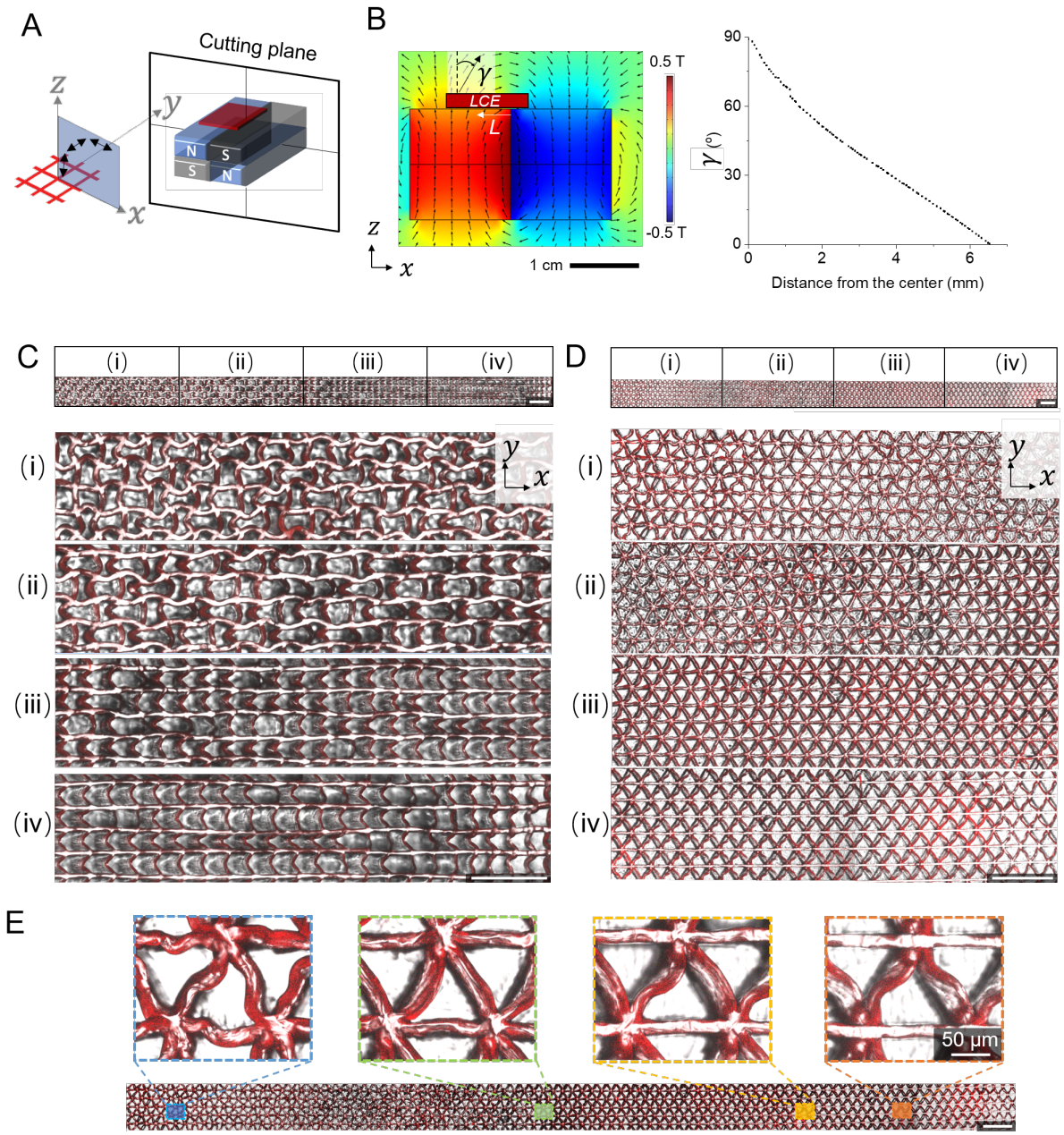

Figure S17: **LCEs cellular structures with spatially varying alignment.** (A) Schematics of the magnetic setup. (B) Numerically predicted magnetic field induced by two magnets placed side-by-side with N pole facing upwards and downwards, respectively. Left: contour plot. Right: evolution of the polar angle of the local magnetic field line as a function of the distance L from the center of magnets setup in the xz-plane along a line 1 mm above the magnet setup (corresponding to the thickness of the PDMS mold). (C-D) Fluorescence micrographs of LCE lattices polymerized in the magnetic field shown in (B) at $T = 135°\text{C} > T_{NI}$. (C) Square lattice with $l/h = 0.6$, $h/t = 6.67$ and $h = 100\mu$m. (D) Triangular lattice with $l/h = 1.9$, $h/t = 4.27$ and $h = 47\mu$m. Scale bars: $= 300\,\mu$m if not specified otherwise.

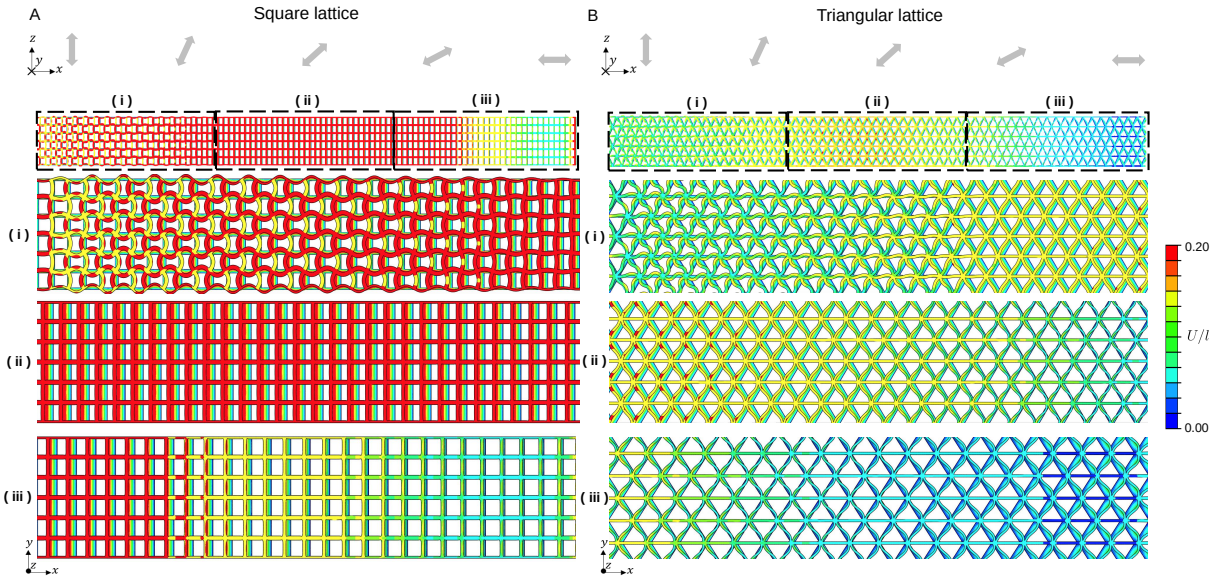

Figure S18: **FE simulations for LCEs cellular structures with spatially varying alignment.** (A) FE results for a square lattice with $l/h = 0.6$, $h/t = 6.67$ and mesogenic director that seamlessly varies from $\gamma = 0°$ to $90°$, while keeping $\alpha = 0°$. The square lattice is infinitely long on the z-direction and counts 100 units along x-direction. (B) FE results for a triangular lattice with $l/h = 1.9$, $h/t = 4.27$ and mesogenic director that seamlessly varies from $\gamma = 0°$ to $90°$, while keeping $\alpha = 0°$. The triangular lattice is infinitely long on the z-direction and counts 120 units along x-direction. The color corresponds to the normalized magnitude of the displacement field in the isotropic phase. A schematic of the mesogenic director alignment continuously varying from z-axis to x-axis is shown at the top.

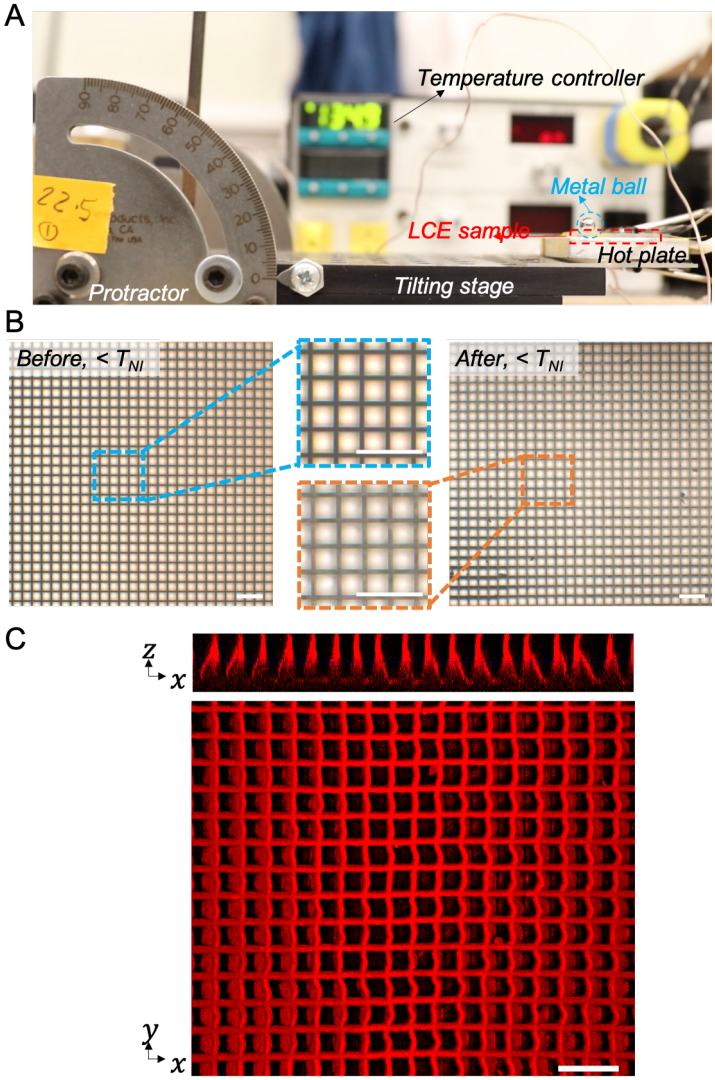

Figure S19: **Frictional properties.** To quantify the direction-dependent frictional properties of our LCE cellular microstructural surfaces, we used sliding angle measurements. (A) A custom-made friction testing setup was built for this purpose, which consists of a tilting stage stationed on top of an optical table, a protractor for reading the sliding angle, a hot-plate fixed to the tilting stage to actuate the LCE structure, and a temperature controller for controlled heating and cooling. In our tests, we first heated LCE films to 135 °C, which is above the N-I phase transition temperature of the LCE and kept the LCE in its deformed state for frictional measurements. A metal ball with 0.5 g weight was gently placed on top of the actuated LCE cellular structure, and the stage was tilted up or down slowly (at $\sim$ 0.25 rad/min) to measure the sliding angle of the metal ball (the smallest tilting angle that the metal ball starts rolling). (B) No noticeable damage of the LCE microstructured surface was observed after 50 cycles of sliding test with metal balls. (C) Fluorescence confocal micrographs of LCE square microcellular structures with $l/h = 0.6$, $h/t = 6.67$, $h = 100\mu$m and the mesogen director that gradually varies from $\gamma = 70°$ to 110°, while keeping α= 0° at $T = 135°$C$> T_{NI}$. This type of sample was use for the tests reported in Fig. 5A-D of the main text. Scale bars: 200 μm

Figure S20: **Effect of the metallic ball on the deformation of the LCE lattices.** We consider an LCE square lattices with $l/h = 0.6$, $h/t = 6.67$ and $l = 60$ μm (where l, h and t denote the length, height and thickness of the plates, respectively) and mesogenic director aligned along the z-axis (i.e. $\alpha = 0°$ and $\gamma = 0°$). In this experiment we placed a metal ball (diameter 5 mm and weight 0.5 g) on the surface of the square lattice at room temperature and slowly increased the temperature to trigger to N-I transition. The images obtained from the inverted microscope (Leica TCS SP5) with the reflection mode at $T = 135°$C reported here show that the portion of the lattice below the metallic ball and far away from it deform very similarly, proving that the presence of ball does not constraint the deformation of the lattice through the N-I phase transition. In the figure the region of the LCE lattice in contact with the ball is highlighted by the white dashed line. The red and green boxes identify the regions inside and outside the contact area, respectively, that we used to compare the deformation behaviors.

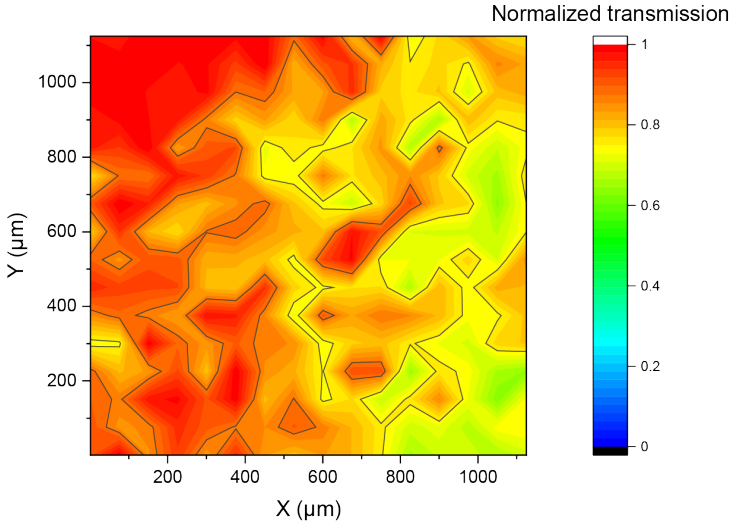

Figure S21: **Transmitted light intensity** Transmitted light intensity profile at $T = 25°$C$< T_{NI}$ for an LCE square lattice with mesogenic director that seamlessly varies from $\gamma = 70°$ to $110°$, while keeping $\alpha = 45°$. Note that in Fig. 5E and F of the main text we report the normalized transmitted light intensity for the same structure at $T > T_{NI}$. To quantify the transmitted light intensity, we imaged the surface with an optical microscope in transmission mode, used ImageJ to average the brightness of the central 30 μm$\times$30 μm area and normalized to the maximum value in each sample to minimize the effect of possible fluctuation of the incident light intensity.

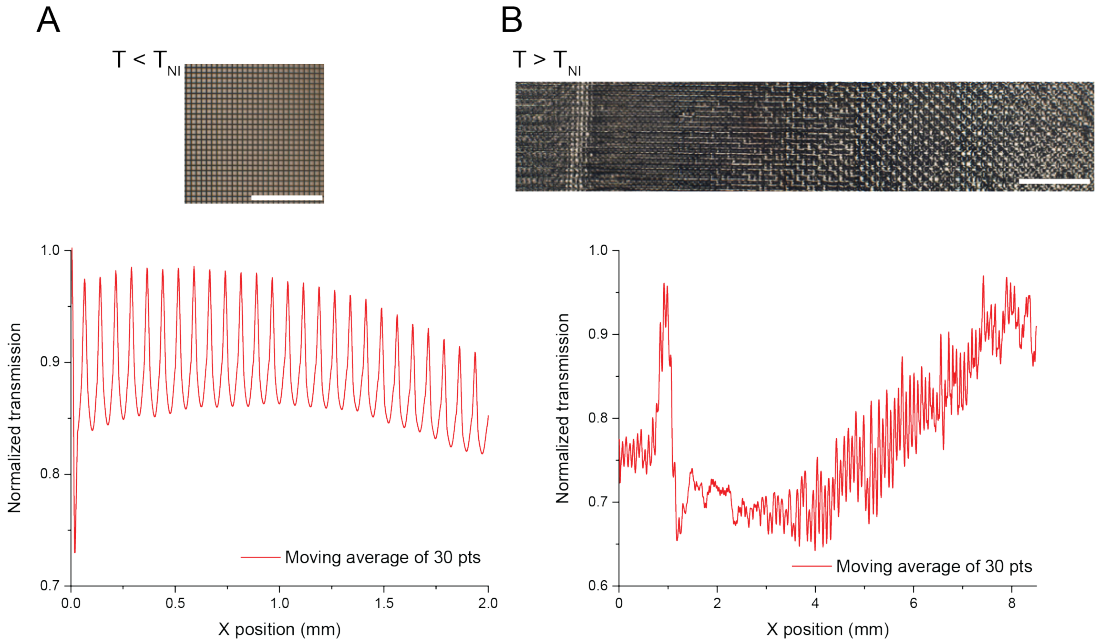

Figure S22: **Average pixel brightness.** Average pixel brightness along vertical lines as a function of their position along the x-axis for a square lattice with mesogenic director that seamlessly varies from $\gamma = -20°$ to 90°, while keeping α= 0° at (A) $T < T_{NI}$ and (B) $T > T_{NI}$. For $T < T_{NI}$, the transmitted light is homogeneous across the sample. Differently, for $T > T_{NI}$ the transmitted light shows a dark-bright-dark-bright pattern following exactly, the spatially varying deformation of the lattice. These results suggest that we can readily control the symmetric profile of the transmission light intensity by patterning mechanical deformation and symmetry breaking in our LCE cellular structures.

S4 Movie Captions

Movie S1: reversible temperature-responsive deformations of LCE square microcellular structures. Heating and cooling of LCE square cellular microstructures. The thermal actuation above the nematic-isotropic phase transition temperature ($T_{NI} \sim 125°$C) and relaxation below T_{NI} was monitored by fluorescent confocal microscopy.

Movie S2: director-dependent deformations of LCE microcellular structures. Various lattice reconfigurations and symmetry breakings of LCE square and triangular cellular microstructures with different LC director alignments. Isotropic/anisotropic buckling, chiral/achiral buckling, shearing, and twisting were observed.

Movie S3: Controlled object transport on LCE microcellular structures. Metal ball sliding on LCE microcellular structures with gradually changing director at $\sim 135°$C. Controlled object stoppage and selective object transport were demonstrated.

S5 References

References

[1] Donald L Thomsen, Patrick Keller, Jawad Naciri, Roger Pink, Hong Jeon, Devanand Shenoy, and Banahalli R Ratna. Liquid crystal elastomers with mechanical properties of a muscle. *Macromolecules*, 34(17):5868–5875, 2001.

[2] Gregory R Fulmer, Alexander JM Miller, Nathaniel H Sherden, Hugo E Gottlieb, Abraham Nudelman, Brian M Stoltz, John E Bercaw, and Karen I Goldberg. Nmr chemical shifts of trace impurities: common laboratory solvents, organics, and gases in deuterated solvents relevant to the organometallic chemist. *Organometallics*, 29(9):2176–2179, 2010.

[3] Yuxing Yao, James T Waters, Anna V Shneidman, Jiaxi Cui, Xiaoguang Wang, Nikolaj K Mandsberg, Shucong Li, Anna C Balazs, and Joanna Aizenberg. Multiresponsive polymeric microstructures with encoded predetermined and self-regulated deformability. *Proceedings of the National Academy of Sciences*, 115(51):12950–12955, 2018.

[4] Mikhail Zhernenkov, Niccolo Canestrari, Oleg Chubar, and Elaine DiMasi. Soft matter interfaces beamline at nsls-ii: geometrical ray-tracing vs. wavefront propagation simulations. In *Advances in Computational Methods for X-Ray Optics III*, volume 9209, page 92090G. International Society for Optics and Photonics, 2014.

[5] Jürgen Küpfer and Heino Finkelmann. Nematic liquid single crystal elastomers. *Die Makromolekulare Chemie, Rapid Communications*, 12(12):717–726, 1991.

[6] P Davidson, D Petermann, and AM Levelut. The measurement of the nematic order parameter by x-ray scattering reconsidered. *Journal de Physique II*, 5(1):113–131, 1995.

[7] Mark T Sims, Laurence C Abbott, Robert M Richardson, John W Goodby, and John N Moore. Considerations in the determination of orientational order parameters from x-ray scattering experiments. *Liquid Crystals*, 46(1):11–24, 2019.

[8] Matthew T Cole, Vito Cientanni, and William I Milne. Horizontal carbon nanotube alignment. *Nanoscale*, 8(35):15836–15844, 2016.

[9] M. Danielsson, D.M. Parks, and M.C. Boyce. Three-dimensional micromechanical modeling of voided polymeric materials. *Journal of the Mechanics and Physics of Solids*, 50(2):351 – 379, 2002.

[10] Johannes T.B. Overvelde and Katia Bertoldi. Relating pore shape to the non-linear response of periodic elastomeric structures. *Journal of the Mechanics and Physics of Solids*, 64:351 – 366, 2014.